Heterogeneous identity, stiffness and growth characterise the shoot apex of *Arabidopsis* stem cell mutants

Running title: Properties of stem cell mutants

Léa Rambaud-Lavigne[1,*], Aritra Chatterjee[2,6], Simone Bovio[1,3], Virginie Battu[1], Quentin Lavigne[4], Namrata Gundiah[5,*], Arezki Boudaoud[1,7,*], Pradeep Das[1,*]

[1]Laboratoire Reproduction et Développement des Plantes, Université de Lyon, ENS de Lyon, UCB Lyon 1, CNRS, INRAE, INRIA, Lyon, France. [2]Centre for BioSystems Science and Engineering, Indian Institute of Science, Bengaluru, India. [3]PLATIM-LyMIC, Université de Lyon, ENS de Lyon, Inserm, CNRS, SFR Biosciences US8 UAR3444, UCB Lyon 1, Lyon, France. [4]Physikalisches Institut, Rheinische Friedrich-Wilhelms-Universität, 53115 Bonn, Germany. [5]Department of Mechanical Engineering, Indian Institute of Science, Bengaluru, India.

Present address: [6]Department of Mechanical Engineering, Birla Institute of Technology & Science, Pilani, Hyderabad Campus, Hyderabad 500078, Telangana, India. [7]LadHyX, CNRS, Ecole Polytechnique, Institut Polytechnique de Paris, 91128 Palaiseau Cedex, France.

[*]Authors for correspondence (lea.rambaud1@ens-lyon.fr, namrata@iisc.ac.in, arezki.boudaoud@polytechnique.edu, pradeep.das@ens-lyon.fr).

ORCID: LRL, 0000-0001-6560-5359; AC, 0000-0002-5318-3459; SB, 0000-0002-9836-6742; VB, 0009-0009-1098-4633; QL, 0000-0003-2326-2604; NG, 0000-0002-9882-5232; AB, 0000-0002-2780-4717; PD, 0000-0002-1179-9044

Key words (3-6): shoot apical meristem, *WUSCHEL*, *CLAVATA*, heterogeneities, morphogenesis, stem cell mechanics

Summary statement: Heterogeneities in cell mechanics, growth, function and identity contribute to buckling in *clavata* mutant shoot apices.

Abstract

Stem cell homeostasis in the shoot apical meristem involves a core regulatory feedback loop between the signalling peptide CLAVATA3, produced in stem cells, and the transcription factor WUSCHEL, expressed in the underlying organising centre. *clavata* mutants display massive meristem overgrowth, which is thought to be caused by stem cell overproliferation, although it is unknown how uncontrolled stem cell divisions lead to this altered morphology. Here we first reveal local buckling defects in mutant meristems, and use analytical models to show how mechanical properties and growth rates may contribute to the phenotype. Indeed, *clavata* meristems are mechanically more heterogeneous than the wild type, and also display regional growth heterogeneities. Furthermore, stereotypical wild-type meristem organisation is lost in mutants, in which cells simultaneously express distinct fate markers. Finally, cells in mutant meristems are auxin responsive, suggesting that they are functionally different from wild-type stem cells. Thus all benchmarks show that *clavata* meristem cells are different from wild-type stem cells, suggesting that fasciation is caused by the disruption of a more complex regulatory framework that maintains distinct genetic and functional domains at the shoot apex.

Introduction

The shoot apical meristem (SAM) is a structure at the growing plant tip that gives rise to all its aboveground tissues. The SAM is sustained by the activity of a small pool of centrally-located undifferentiated stem cells in the slow-dividing central zone (CZ). Through successive divisions, their daughter cells exit from the CZ into the surrounding peripheral zone (PZ), where they may differentiate into lateral organs, such as leaves or flowers. The CZ is itself maintained via the activity of the underlying organising centre (OC) (Laux et al., 1996).

The regulatory network driving stem cell maintenance in *Arabidopsis* is well studied. At its core is a feedback loop between WUSCHEL (WUS), a homeobox transcription factor expressed in the OC, and CLAVATA3 (CLV3), a signalling peptide expressed in the CZ (Brand et al., 2000; Clark et al., 1995; Laux et al., 1996; Schoof et al., 2000). WUS moves from the OC to the CZ and induces stem cell identity by directly binding to the *CLV3* promoter and activating its expression (Daum et al., 2014; Yadav et al., 2011). In turn, CLV3 binds receptors, such as the leucine-rich-repeat receptor-like kinase CLV1 (Clark et al., 1997) or the receptor-like proteins CLV2 (Kayes and Clark, 1998) and CORYNE (CRN) (Fletcher et al., 1999; Jeong et al., 1999; Miwa et al., 2008; Müller et al., 2008). Signalling from these ligand-receptor complexes ultimately leads to the downregulation of *WUS* in the OC (Miwa et al., 2008; Müller et al., 2006). The absence of WUS activity leads to SAM arrest early in development (Laux et al., 1996), whereas the loss of the *CLV* genes results in a vast enlargement of the SAM (Clark et al., 1993; Clark et al., 1995; Kayes and Clark, 1998) through a phenomenon called fasciation. Several instances of fasciated tissues have been observed in the wild, as well as in crop plants, including beef tomatoes and the maize *fasciated ear2* mutant (Taguchi-Shiobara, 2001). It is thought that fasciation is caused by stem cell overproliferation in the CZ (Brand et al., 2000; Busch et al., 2010; Dao et al., 2022; Kwon et al., 2005; Lenhard and Laux, 2003; Müller et al., 2008; Nimchuk et al., 2011; Whitewoods et al., 2018; Wu et al., 2005), or conceivably, by lower rates of cell transit from the CZ to the PZ (Laufs et al., 1998).

Over the years, *CLV3* has been the only known genetic marker to study stem cells at the shoot apex (Müller et al., 2006; Reddy and Meyerowitz, 2005), including for analysing *clv* mutants. While microarray analyses have uncovered several other genes that are enriched in the CZ (Aggarwal et al., 2010; Busch et al., 2010; Yadav et al., 2009), none have been extensively characterised. More recently, atomic force microscopy (AFM) experiments,

which measure cellular mechanical properties, revealed that *CLV3*-expressing cells are stiffer than surrounding PZ cells, and that the onset of *CLV3* expression in flowers coincides with an increase in cell wall stiffness (Milani et al., 2014). Thus, although stem cell identity is both spatially and temporally associated with increased cell stiffness (Milani et al., 2014), it is unknown how these mechanical patterns are altered when stem cell regulation is perturbed.

The core stem cell regulatory network is also influenced by hormone signalling, including cytokinin and auxin (Gordon et al., 2009; Busch et al., 2010). Exogenous cytokinin treatment phenocopies the *clv* mutant by increasing *WUS* expression and decreasing *CLV1* expression (Lindsay et al., 2006). While exogenous auxin treatment induces organogenesis markers in the PZ, the CZ itself remains unaffected, displaying reduced responsivity to auxin (de Reuille et al., 2006). Whereas in the PZ, the auxin response factor MONOPTEROS (MP) activates the expression of lateral organ identity genes in an auxin-dependent manner (Berleth and Jürgens, 1993; Bhatia et al., 2016; Hardtke and Berleth, 1998; Yamaguchi et al., 2013), it also functions to repress CZ genes that are themselves activators of *CLV3* expression (Luo et al., 2018; Zhao et al., 2010). Despite these advances, it remains unclear how auxin signalling is perturbed in *clv* mutants, and furthermore, whether this plays a direct role in generating the fasciated *clv* phenotype.

In this study, we use quantitative approaches to study the effects of the loss of proper stem cell regulation that reveal hitherto unobserved cellular and tissular phenotypes, such as cell size and local surface curvature in *clv* mutant SAM. Analytical mechanical models predict that heterogeneities in stiffness and/or growth regimes are sufficient to account for the changes in surface curvature observed in the mutant. We provide experimental support for these predictions by showing that both growth and mechanical properties display regional differences, which are likely caused by the chimeric identities of mutant meristematic cells. Finally, auxin-response quantifications in *clv* meristems reveal a behaviour similar to undifferentiated WT PZ cells, rather than to stem cells.

Results

Altered cellular and tissular properties characterise fasciated *clv* SAM

In order to better understand the defects associated with abnormal stem cell regulation, we first quantified the highly fasciated phenotype of the canonical *clv3-2* allele (Clark et al.,

120 1995). WT shoot meristems displayed a stereotypical dome shape, whereas *clv3-2*
121 meristems comprised a large centrally-located bulge and two or more arm-like outgrowths
122 that elongate laterally (Fig. 1A, B, Fig. S1A-C). Further analysis revealed that the central
123 areas were usually devoid of any discernible cellular organisation, whereas the lateral arms
124 were often composed of cell files (Fig. S1D, E). These results were consistent across three
125 *clv1* and four *clv3* alleles (Fig. S1A-C) in our growth conditions, although individual plants
126 showed varying degrees of fasciation.
127
128 We also detected novel floral phenotypes. First, we frequently observed radially
129 symmetrical, filament-like organs either growing on the flanks of the meristem or within the
130 inflorescence itself (Fig. 1C, D). Such filaments were recently noted as aborted flowers in
131 double mutants of *clv2* or *clv3* and with auxin biosynthesis mutants (John et al., 2023; Jones
132 et al., 2020). Secondly, while the majority (>90%) of flowers showed previously described
133 phenotypes of supernumerary organs (Clark et al., 1993; Clark et al., 1995), the rest
134 displayed two types of opposing phenotypes. One group of flowers bore two or three sepals
135 and petals, a single stamen and no carpels (Fig. 1C, E, F), reminiscent of the inner-whorl
136 phenotypes of *wus* mutants (Laux et al., 1996), whereas a second group displayed a tubular
137 phenotype with fused sepals (Fig. 1C). These flowers were distinctly smaller than those with
138 supernumerary organs. These novel floral phenotypes were observed in all *clv1* and *clv3*
139 alleles.
140
141 Because it had been suggested that cell size in *clv* mutants differs from the WT (Laufs et
142 al., 1998), we wondered whether we could use such changes in cellular morphologies to
143 further characterise the mutant phenotypes described above. We quantified cell size in two
144 ways: firstly, we calculated cell areas by acquiring images of meristems from WT and
145 multiple *clv1* and *clv3* SAM, and extracting slices near the midpoints of cells in the L1 and
146 L2 layers, which we then segmented using the MorphoGraphX software (Barbier de Reuille
147 et al., 2015). In WT SAM, the average area was similar in both cell layers, with L1 cells at
148 23.9 ± 5.8 μm^2 and L2 cells at 24.5 ± 7.2 μm^2 (Fig. 1G). In contrast, *clv3-2* mutants exhibited
149 significant differences in the L1 and L2, with L2 cells on average 69% larger than L1 cells –
150 31.2 ± 9.8 μm^2 in the L2 versus 18.4 ± 5.3 μm^2 in the L1 (Fig. 1G). Secondly, we measured
151 cell volumes in WT and *clv* SAM, by generating 3D reconstructions using the MARS pipeline
152 (Fernandez et al., 2010), which involves imaging samples from multiple angles and fusing
153 those images to generate high-resolution images that are then segmented in 3D (Fig. S1F).
154 Consistent with our findings for cell areas, we found that while L1 and L2 cells had

155 comparable volumes in the WT (136.5 ± 40.5 μm^3 and 148.7 ± 44.6 μm^3, respectively), L2
156 cells in *clv3-2* SAM were almost twice as large as L1 cells (249.1 ± 130.7 μm^3 vs 129.5 ±
157 40.9 μm^3) (Fig. 1H). Similar trends were observed for cell size in other *clv1* and *clv3* alleles,
158 suggesting that altered cell morphology is a general feature of these mutants (Fig. S1G).
159
160 We had noticed that meristems in *clv3* mutants are less smooth than WT meristems. We
161 quantified this by measuring curvature at the sample surface, using a method that detects
162 the outer surface in MARS-reconstructed 3D meristems (Kiss et al., 2017). We used
163 MorphoGraphX to calculate curvature within a 10-μm radius of every pixel on the surface.
164 In WT plants, the meristem dome and young flowers were regions of uniformly positive
165 curvature, separated by clearly defined boundary areas with negative curvature (Fig. 1I).
166 However, the imaged areas of *clv1* and *clv3* SAM, which are distant from the regions where
167 flowers form, displayed a much more variable surface curvature, with crests and troughs of
168 varying shapes and depths distributed throughout (Fig. 1J). Together, our data reveal that
169 *clv* mutants exhibit abnormal cellular traits and buckling defects that contrast with the
170 stereotypical characteristics of WT meristems.
171
172 **Morphoelastic models reveal how growth and stiffness contribute to tissue buckling**
173 To elucidate a theoretical basis for the buckling defects of *clv* mutants, we next generated
174 analytical models of SAM development using a growth and remodelling framework (Goriely,
175 2017). Specifically, we adapted a model developed to explore the biomechanical basis of
176 morphogenesis in unrelated systems that display similar buckling behaviour to that observed
177 in *clv* mutants (Almet et al., 2019; Moulton et al., 2013). We modelled the SAM as an axially
178 growing planar elastic rod (the outer L1 layer), attached to an elastic foundation (the inner
179 layers), and clamped at the two ends (Fig. S2). We used the theoretical model to explore
180 how growth stretch, a proxy for tissue growth, and/or mechanical properties, a proxy for
181 cellular stiffness, might contribute to the altered morphology of *clv* mutants (see
182 Supplementary Materials and Methods).
183
184 First, we used linear stability analysis to plot the output shapes when either the growth
185 stretch (γ) alone or the system stiffness ($\hat{k}$, the ratio of foundation and rod stiffnesses) was
186 varied. These analyses showed that when the foundation and rod had similar mechanical
187 properties ($\hat{k}$ = 1) and when growth stretch was at a low, subcritical value (γ^*_{inf}= 5.82), the
188 output shape resembled the smooth dome of a WT meristem (Fig. 2A). In contrast, when
189 the growth stretch was raised to a near-critical point (γ^*_{inf}= 8.99), the size of the dome

increased, while remaining smooth. A further increase in growth stretch generated various modes of buckling (Fig. 2A) that broadly capture the curvature defects of *clv* mutants. Next, we investigated the role of system stiffness ($\hat{k}$) on SAM morphology, by varying stiffness within a background of constant growth stretch (γ^* = 12.23) (Fig. 2B). Whereas no buckling was visible for higher values of stiffness ($\hat{k} \geq 1$), lowering it ($\hat{k}$ = 0.5) led to the appearance of buckling in the rod (Fig. 2B), which was similar to those obtained using growth values above the critical point (Fig. 2A). Taken together, these analytical results indicate that in a biological context, cellular growth and stiffness characteristics could influence tissue architecture of the SAM.

In contrast to the symmetrical shapes obtained above, *clv* mutant SAM in fact display highly variable buckling, such that the positions, numbers and amplitudes of folds differ within, and between, individual mutant meristems. We reasoned that this variability might result from local differences in growth, stiffness or both. To investigate the effects of such heterogeneities on buckling, we replaced constant growth stretch or system stiffness with one of three distinct functions to generate differential distributions across the rod (Fig. 2C). Indeed, all three functions generate variable buckling over the length of the rod when either growth stretch (Fig. 2D, Fig. S3B-B') or system stiffness (Fig. 2E) is spatially distributed, with the resulting shapes often closely resembling the asymmetry and variable buckling amplitudes visible in sections through various *clv* SAM in the literature. These results suggest that local differences in growth or stiffness within the SAM could explain the phenotypes of *clv* mutants.

Finally, we asked whether variations in system stiffness and growth stretch could act together to generate even greater differences in buckling characteristics. To address this question, we used a cosine spatial growth stretch distribution and examined how buckling was affected when system stiffness ($\hat{k}$) was varied between 0.5 and 1.5. Indeed, for identical distributions of growth, rod buckling varied locally as a function of stiffness (Fig. 2F); these analyses suggest that small changes at the cellular level could alter shape locally.

Taken together, our results indicate that growth and mechanical traits are sufficient to describe the differences in meristem shape between WT and *clv* SAM. Furthermore, local variations of these two cellular parameters could lead to the local curvature defects observed in *clv* meristems.

225 **Heterogeneous growth correlates with buckling in *clv* mutants**
226 We tested predictions from the analytical model by first examining whether *clv* mutants
227 display local heterogeneities in growth and, more specifically, whether these differences
228 correlate with areas of differential curvature. We did this by dissecting WT and *clv3-7*
229 meristems, placing them on culture medium and imaging them once a day over 72 hours by
230 confocal microscopy. We then segmented the image stacks, tracked cell lineages, and
231 analysed cell size, growth and curvature over the tissue (Fig. 3A-H, Fig. S4A-C). In the WT,
232 cells had a mean size of 22.8 $\pm$ 5.8 μm^2 at the start of the experiment and over 72 hours
233 their daughters had grown 5.5 $\pm$ 1.3 fold (Fig. 3A-C). Of these, lineages that remained
234 entirely within the meristem dome grew 4.9 $\pm$ 1.1 fold. In contrast, cells at the very top of the
235 *clv3* meristem had an initial size of 17 $\pm$ 6.2 μm^2 and had grown 1.5 $\pm$ 0.3 fold over 72 hours
236 (Fig. 3E-G).
237
238 In the WT, a gradient of differential growth is observed from the centre to the periphery of
239 the meristem, whereas in the mutant, groups of cells with varying growth rates are seemingly
240 scattered across the enlarged meristem (Fig. 3C, G). To determine whether this observation
241 is relevant in the context of buckling in *clv* meristems, we then measured curvature at the
242 surface of WT and mutant samples, determined the mean value per cell (Fig. 3D, H, Fig.
243 S4C), and tested correlations between cell size, growth rate and local curvature (Fig. 3I-L,
244 Fig. S4D-E). WT meristems showed no significant correlations between any parameters
245 (Pearson's correlation coefficients (r) between: growth and curvature, r = -0.17, p = 0.18;
246 size and curvature, r = -0.035, p = 0.79; growth and size, r = -0.23, p = 0.07) (Fig. 3I-J, Fig.
247 S4D). *clv3* mutants, however, displayed significant moderate or strong positive correlations
248 between all parameters (Pearson's correlation coefficients between: growth and curvature,
249 r = 0.59, p < 0.001; size and curvature, r = 0.41, p < 0.001; growth and size, r = 0.36, p <
250 0.001) (Fig. 3K-L, Fig. S4E). These analyses show that in *clv3* mutants, both cell size and
251 growth rate are variable across the tissue and are linked to local buckling characteristics.
252
253 **Loss of *CLV* activity is associated with reduced and variable epidermal cell stiffness**
254 In addition to growth heterogeneity, our analytical models predicted that buckling is also
255 dependent on stiffness changes in the SAM. We had previously shown that *CLV3*-
256 expressing CZ cells are stiffer than PZ cells (Milani et al., 2014). Because the *clv* phenotype
257 is thought to be caused by stem cell overproliferation, we predicted that cells in *clv*
258 meristems might bear higher values of stiffness. To test this, we probed epidermal cells in
259 WT, *clv1* and *clv3* SAM using atomic force microscopy (AFM), as published (Milani et al.,

260 2014; Beauzamy et al., 2015) (Fig. S5A-D). The resultant force-displacement curves at each
261 measured point from individual AFM scans were analysed to determine the apparent
262 Young's modulus up to a depth of 100 nm, and these values were subsequently corrected
263 to remove artefacts caused by local slope (Fig. 4A-D). The data were either pooled and
264 plotted as density curves (Fig. 4E, F) or analysed by individual scans as box plots (Fig. 4G,
265 H). When compared to the appropriate WT accession, we found that both *clv3-2* (Fig. 4E,
266 G) and *clv1-8* cells (Fig. 4F, G) were significantly softer, with apparent Young's moduli that
267 were 15-20 % lower than WT cells (Fig. 4G, Fig. S5E, Table S1, Table S2).
268
269 While these results show that *clv* mutant SAM bear different physical characteristics to WT
270 cells, they do not reveal whether they also display greater heterogeneity. To test this, we
271 plotted standard deviation values for each scanned region by genotype (Fig. 4H) and found
272 that *clv* mutant samples indeed display a significantly greater variability in values of apparent
273 Young's moduli when compared to the WT. This altered regime is also visible in the density
274 plots (Fig. 4E, F), where mutant distributions are notably broader than in the WT.
275 Furthermore, scatter plots of the dataset show that mean and standard deviation are not
276 correlated (Fig. S5F-I). Consistent with our analytical models, these results suggest that
277 altered local stiffness and increased heterogeneity could indeed contribute to tissue buckling
278 in *clv* mutants.
279
280 **Genetic domain separation is lost in *clv* SAM**
281 We reasoned that the local heterogeneities in growth and stiffness described above might
282 be caused by underlying variations in genetic identity. To examine this, we first retested the
283 expression patterns of OC and CZ markers using mRNA *in situ* hybridisation assays in WT
284 and different *clv3* alleles. We used *WUS* to examine OC identity (Laux et al., 1996; Mayer
285 et al., 1998), whereas for the CZ, we tested several genes previously identified as enriched
286 in *CLV3*-expressing cells (Yadav et al., 2009) and retained the *APUM10* gene, which
287 encodes a member of the Puf family, with a conserved Pumillio homology domain (Tam et
288 al., 2010). *APUM10* was observed in a few centrally-located cells of the L1 and L2 in WT
289 SAM (Fig. 5A), and *WUS* in an underlying group of cells (Fig. 5B). In *clv3* mutants, we
290 detected both *APUM10* and *WUS* in broad domains occupying almost the entire meristem,
291 with *APUM10* expressed principally in the L2 layer (Fig. 5C, C') and *WUS* in deeper layers
292 (Fig. 5D-D'). However, both genes were expressed in a discontinuous manner, with no
293 detectable expression in scattered groups of cells. An inspection of published expression

294 data in *clv* mutants revealed that such patchy expression was frequently visible, but had
295 gone unremarked (Brand et al., 2000; Kinoshita et al., 2015; Schuster et al., 2014).
296
297 One explanation for why some patches of cells in *clv3* mutants expressed neither CZ nor
298 OC identity was that they might instead bear other identities. To test this, we localised mRNA
299 for the *MP* gene (Hardtke and Berleth, 1998), which is expressed mainly in the WT PZ (Zhao
300 et al., 2010) (Fig. 5E). In *clv* SAM, the PZ is thought to be restricted to areas at the base of
301 the enlarged dome, in the region where flowers form. However, we found that in *clv3*
302 mutants, *MP* is expressed in a broad and patchy manner (Fig. 5F-F'), similarly to the
303 *APUM10* and *WUS* patterns. Taken together, our results suggest that identities of the three
304 meristematic zones are present in overlapping groups of cells in *clv* apices.
305
306 We thought it possible that normal domain organisation might exist at a more local level. In
307 order to investigate the positions of the OC and PZ markers relative to the CZ marker within
308 *clv* SAM, we performed pairwise *in situ* hybridisations using alternating sections from
309 individual fixed meristems, with one probe used on even-numbered sections, and a second
310 on odd-numbered sections. In WT meristems, the *APUM10*, *WUS* and *MP* expression
311 domains were never detected in similar regions within adjacent sections (Fig. 5G, G', J, J').
312 However in *clv3* mutants, *APUM10* and *WUS* expression overlapped across the entire SAM
313 (Fig. 5H-I', Fig. S6), except for a few areas where *APUM10* was observed but *WUS* was not
314 (Fig. 5H', I') and rare areas where *WUS* was expressed without *APUM10*. Similarly in *clv3*
315 mutants, *APUM10* and *MP* were expressed in overlapping patterns, except for a few areas
316 where *MP* was expressed without *APUM10* (Fig. 5K-L', Fig. S7) and no instances where
317 *APUM10* was expressed without *MP*. We also observed a few cell patches devoid of any
318 signal.
319
320 Together, these results show that *clv3* meristems comprise a heterogeneous group of cells
321 with mixed genetic identities, rather than a homogeneous population of stem cells.
322 Furthermore, we observed similar expression patterns in SAM from other alleles of *clv1* and
323 *clv3* (Fig. S8), suggesting that chimeric cell identities are a general feature of fasciated *clv*
324 meristems.
325
326 **Exogenous auxin elicits a strong response in *clv3* meristems**
327 Because cells in fasciated *clv3* SAM displayed traits not usually associated with stem cells,
328 such as chimeric cell identities and reduced stiffness, we wished to better understand if they

329 were also functionally different from stem cells. We chose auxin response as a functional
330 readout for the following reasons: firstly, auxin-associated genes are differentially expressed
331 in WT and *clv3* mutants (John et al., 2023). Secondly, a key aspect of organogenesis at the
332 shoot apex is the presence of a CZ that is refractive to auxin signalling (de Reuille et al.,
333 2006; Douady and Couder, 1996; Galvan-Ampudia et al., 2020; Vernoux et al., 2011),
334 suggesting that auxin insensitivity is an indicator of stem cell identity. Thirdly, MP, a polarity
335 regulator of the auxin efflux transporter PIN1, which itself promotes auxin accumulation and
336 drives organogenesis (Bhatia et al., 2016), is misregulated in *clv* mutants (Fig. 5E, F).
337
338 In order to test how *clv* mutants respond to auxin, we dissected shoot apices from WT, *clv1*
339 and *clv3* plants carrying the auxin signalling reporter, *pDR5rev::GFPer*, and treated them
340 with exogenous auxin as described (Galvan-Ampudia et al., 2020), while monitoring
341 expression every 24 hours. As is well understood, in 100 % of WT samples prior to
342 treatment, GFP was localised in small groups of cells corresponding to the positions of floral
343 anlagen, accompanied by low expression in the geometric centre of the SAM (Fig. 6A). 24
344 hours later, we observed high levels of GFP throughout the periphery of the SAM and in
345 internal layers, whereas expression levels at the centre remained low (Fig. 6B). *clv*
346 meristems differed from the WT in that prior to auxin treatment, we detected only very basal
347 levels – several thousand-fold lower than in the WT – of GFP (Fig. 6C), whereas 24 hours
348 after treatment, a clear response was visible in all samples (Fig. 6D). More specifically, a
349 minority of meristems (1 out of 11 *clv3* SAM) showed high levels of GFP in both outer and
350 inner layers (Fig. S9A, B), whereas in all other samples (10 out of 11 *clv3*, and 5 out of 5
351 *clv1*) expression levels were variable and patchy in outer layers, and high in inner layers
352 (Fig. 6D).
353
354 We next quantified this response by segmenting image stacks of WT (Fig. 6E, F) or mutant
355 (Fig. 6I, J) meristems before and after auxin treatment, and extracted average fluorescence
356 values per cell (Fig. 6G, H, K, L). For each cell, we then calculated the ratio of expression
357 between the two time points, normalised this across the sample, and compared values in
358 the mutant to values for cells in either the geometric centre or the periphery of WT
359 meristems. A histogram of cell signal intensities shows that before auxin treatment, 22 % of
360 WT cells and 100 % of mutant cells were in a low-expressing category of signal intensities
361 under an arbitrary threshold set to 1/10th of the highest value (Fig. S9C). After treatment
362 with auxin, only 6.4 % of WT and 5.9 % of mutant cells remained in this category, suggesting
363 that the *clv* meristem responded to exogenous auxin in a similar manner to the WT.

364 Furthermore, plots of normalised intensity change per lineage show that cells from the
365 putative WT CZ and WT PZ, as well as from the *clv3* mutant had significantly different
366 distributions from each other, although qualitatively the mutant resembled the PZ more than
367 the CZ (Fig. 6M). Similar results are obtained for *clv1* mutants carrying the *DR5* reporter
368 (Fig. S9D, E). Taken together, these results show that cells in *clv* mutant SAM are capable
369 of responding to auxin signalling, an output more associated with the WT PZ, where organ
370 specification occurs.
371
372
373 **Discussion**
374 The development of fasciated meristems due to the loss of *CLV* activity in *Arabidopsis* shoot
375 apical stem cells has generally been interpreted as being caused by a massive increase in
376 stem cell numbers (Brand et al., 2002; Busch et al., 2010; Dao et al., 2022; Kwon et al.,
377 2005; Lenhard and Laux, 2003; Müller et al., 2006; Nimchuk et al., 2011; Whitewoods et al.,
378 2018; Wu et al., 2005). Direct experimental evidence for this comes principally from a *CLV3*
379 transcriptional reporter, which is expressed throughout the enlarged meristem of *clv* mutants
380 (Brand et al., 2002; Reddy and Meyerowitz, 2005). However, because WUS protein is known
381 to directly activate *CLV3* transcription (Yadav et al., 2011), and because *WUS* is expressed
382 throughout *clv* meristems (Schoof et al., 2000), it is not surprising that *CLV3* reporter
383 expression is broad in *clv* mutant. We suggest that the *CLV3* reporter might thus not be an
384 appropriate marker to study cell identity in *clv* meristems. Furthermore, the use of the *CLV3*
385 promoter for various misexpression studies of the role of stem cells in meristem
386 maintenance might be inappropriate.
387
388 An alternate way of deciphering regional identities is by characterising cellular properties,
389 which we have done using recently-developed approaches to precisely quantify cell
390 volumes, areas and surface curvatures. Although we show that epidermal and subepidermal
391 cell sizes in *clv* meristems are different from the WT, the effect of such changes on meristem
392 structure is difficult to estimate. One possibility is that they generate a higher frequency of
393 cell boundary overlaps between the L1 and L2 layers, which could generate a mechanically
394 fragile structure, akin to a wall built with smaller cells in one layer and much larger bricks in
395 the next.
396
397 Our analytical model attempts to explain meristem morphology through a mechanical
398 framework, in contrast to various other modelling studies, which have shed light on different

399 aspects of meristem shape and function, such as the role of auxin in phyllotactic patterning
400 or homeostasis of the CLV-WUS feedback loop (Banwarth-Kuhn et al., 2022; Battogtokh
401 and Tyson, 2022; Chickarmane et al., 2012; Fujita et al., 2011; Galvan-Ampudia et al., 2020;
402 Gruel et al., 2016; Heisler et al., 2005; Jönsson et al., 2005; Jönsson et al., 2006; Klawe et
403 al., 2020; Michael et al., 2023; Plong et al., 2021). Our results suggest that the specific
404 buckling-like patterns displayed by *clv* mutants can be explained by a combination of local
405 heterogeneities in growth rates and in mechanical properties. Indeed, we show that mutant
406 tissues are 15-20% less stiff than the WT and display a wider range of stiffnesses. We had
407 expected *clv* cells to be stiffer than WT cells, because *CLV3*-expressing WT CZ cells are
408 stiffer than PZ cells (Milani et al., 2014), and because the prevailing view in the literature is
409 that cells in *clv* SAM bear stem cell identity. Our findings indicate that this view might be
410 incorrect.
411
412 A wavy surface can arise from buckling with the epidermis growing more than subepidermal
413 layers, or from differences along the epidermis, with accelerated growth in bumps or growth
414 constriction in the valleys. The results presented here cannot fully distinguish between these
415 scenarios. However, a recent study revealed that cellular turgor pressure is anticorrelated
416 to the size and number of neighbours of a given cell, but is correlated to its growth rate, such
417 that smaller cells with fewer neighbours display higher pressure and higher growth (Long et
418 al., 2020). In this context, our results showing a large epidermal-to-subepidermal cell size
419 differential suggest that subepidermal cells in *clv* mutants are less stiff and grow less than
420 the significantly smaller epidermal cells, which is consistent with predictions from our
421 analytical model, that buckling occurs when inner layers are less stiff than the L1. A further
422 experimental validation of this would require techniques to measure stiffness or pressure in
423 internal layers.
424
425 That tissue-level shape robustness emerges from cell growth and cell size variability
426 averaged through space and time has been shown in multiple contexts (Hervieux et al.,
427 2016; Hong et al., 2016; Kamimoto et al., 2016; Tsugawa et al., 2017). Interestingly we find
428 that overall, *clv* mutants grow at a much lower rate than the WT, indicating that the enlarged
429 meristem of mature plants is likely to be a result of the amplification of early changes through
430 time, rather than due to increased proliferation later in development. A recent study has
431 shown that impairing cellulose synthesis decreases both cell proliferation and cell stiffness,
432 leading to smaller SAM, and that in the context of a *clv1* mutant, it results in a dramatic
433 reduction of the fasciated phenotype (Sampathkumar et al., 2019). Since we now show that

434 *clv* mutants themselves have slower growth and reduced stiffness, it is not evident how a
435 further reduction of both parameters could result in an amelioration of the *clv* phenotype. A
436 recent study shows that cell expansion in parts of the meristem can be accounted for by
437 stress-dependent orientation of cell division planes (Banwarth-Kuhn et al., 2022). Thus the
438 early effects of lowered cellulose synthase activity in reducing tensile stress may prevent
439 the *clv* phenotype from developing in plants with impaired cellulose synthase activity.
440 Furthermore, an important distinction is that our study focuses on local buckling, rather than
441 on global fasciation.
442
443 Mechanical and growth heterogeneities in *clv* mutants may be caused by underlying
444 perturbations in genetic patterns. Variable and patchy expression of CZ and OC markers
445 are in fact visible in the literature (Brand et al., 2000; Reddy and Meyerowitz, 2005; Schlegel
446 et al., 2021; Schoof et al., 2000), although few studies have remarked upon, or interpreted,
447 these data. It is unclear precisely how this pattern arises in the mutant and how it behaves
448 over time. Furthermore, chimeric identities might exist in regions of fate transit within WT
449 meristems, for instance at the CZ-PZ or the PZ-flower boundaries. In this context, it would
450 be informative to look at the expression of a related negative feedback loop that functions
451 specifically in the PZ (Schlegel et al., 2021).
452
453 In the absence of external stimuli, cells in *clv* meristems clearly do not undergo
454 differentiation, like WT CZ cells. However, we show that cells in *clv* meristems are more akin
455 to WT PZ cells in their capacity to respond to auxin signalling, perhaps due, at least in part,
456 to their heterogeneous identities. Bhatia et al. (Bhatia et al., 2016) show that for
457 organogenesis to occur, spatial differences in MP are a necessary condition. This is indeed
458 the case in *clv* mutants, where *MP* expression is both broad and patchy, suggesting that
459 improper auxin distributions or signalling contribute to the *clv* phenotype. It is thus unclear
460 why organogenesis is affected in *clv* plants. One possibility is that CLV signalling might
461 regulate auxin activity directly, such as in the moss (Nemec-Venza et al., 2022).
462 Alternatively, because auxin accumulation in space and time is crucial for organogenesis
463 (Galvan-Ampudia et al., 2020; Reddy and Meyerowitz, 2005; Reinhardt et al., 2000; Vernoux
464 et al., 2000), it is possible that the abnormal shapes of *clv* SAM do not allow proper auxin
465 patterns to be generated over most of the meristem. In this model, an initial change in the
466 geometry of *clv* SAM would lead to perturbations in auxin fluxes, thereby inhibiting the
467 production of lateral organs, which are a major auxin source (Shi et al., 2018). The presence
468 of fewer primordia would generate even lower auxin levels in the SAM and lead to an

469 increase in size (Shi et al., 2018). In support of this, the novel floral phenotypes we reveal
470 are reminiscent of certain auxin pathway components (Cheng et al., 2006). Furthermore, it
471 was recently shown that *clv* SAM are sensitised to auxin levels (John et al., 2023). A detailed
472 analysis of auxin fluxes and auxin signalling in *clv* meristems will be necessary to understand
473 the role of auxin in fasciation.
474
475 Taken together, all examined parameters in this study show that cells in *clv* SAM are
476 different from WT CZ cells, and that they do not fit the current idea of typical stem cells. We
477 suggest that stem cell identity needs to account for genetic, mechanical and functional
478 parameters. Reporters for diverse cellular properties, as well as detailed real-time analyses,
479 will help elucidate how chimeric identities arise and what their effects are on plant
480 architecture.
481
482
483 **Materials and methods**
484 *Plant material and culture conditions*
485 The following plant lines were used in this study: L*er* and Col-0 as wild types, *clv3-2* (Clark
486 et al., 1995), *clv3-7* (Fletcher et al., 1999), *clv1-8* (Medford et al., 1992), *pCLV3::GFPer*
487 (Reddy and Meyerowitz, 2005), *pDR5rev::GFPer* (Friml et al., 2003), *pDR5::3xVENUS-N7*
488 (Vernoux et al., 2011), and *pUBQ10::LTI6b-TdTomato* (Shapiro et al., 2015).
489
490 Seeds were sown on soil, and placed in short-day conditions (8 hrs light, 20°C, 50-60%
491 humidity and 16 hrs dark, 16°C, 50-60% humidity) for ten days. Seedlings were then
492 transplanted into individual pots and placed back into the short-day conditions growth
493 chamber. One month after transplantation, plants were transferred from short-day to long-
494 day conditions (16 hrs light period, 20°C, 60% humidity and 8 hrs dark period, 19°C, 60%
495 humidity) until flowering, which is when we used plants for further experiments (in situ
496 hybridisations, confocal microscopy, AFM). The light sources were LED fixtures (Valoya,
497 C75, spectrum NS12), with an intensity of 150 $\mu mol.m^{-2}.s^{-1}$.
498
499 *CRISPR mutagenesis of CLV3*
500 Generation of *CLV* mutants was carried out using a multiplexing CRISPR system (Stuttmann
501 et al., 2021) to create the *clv3-21* allele in Col-0 plants carrying a *pUBQ10::LTI6b-tdTomato*
502 reporter construct. Two guide RNAs targeting *CLV3* (5'-gATCTCACTCAAGCTCATGC-3'
503 and 5'-TCAAGGACTTTCCAACCGCA-3') were designed using the Benchling software

504 (www.benchling.com) and placed under the control of the *U6* promoter in the pDGE333 and
505 pDGE334 'level 0' shuttle vectors as described (Stuttmann et al., 2021). These sgRNA
506 constructs were subsequently assembled in the CAS9-carrying pDGE347 binary vector,
507 along with the FAST-red marker (fluorescence-accumulating seed technology) (Shimada et
508 al., 2010) and the *bialophos resistance* gene (BAR) that confers resistance to glufosinate
509 ammonium (Basta) for positive selection of transformants. T1 generation seeds that were
510 positive for FAST-red were germinated on plates containing Basta and target genes from
511 putative transformants were sequenced by Sanger sequencing, screened for *clv*-like
512 phenotypes in the T2 and T3 generations and resequenced to generate independent
513 homozygous lines. The *clv3-21* allele carries an insertion of an A after the second base pair
514 of exon 2, leading to a frameshift at position 24 of the CLV3 protein.
515
516 *Bright field photos*
517 Bright field photographs of plants were taken with a binocular Nikon SMZ18 equipped with
518 an objective Nikon SHR Plan Apo 1X WD:60, and an ORCA-Flash4.OLT camera.
519
520 *Plant dissection and preparation for confocal microscopy*
521 SAM were grown on soil and dissected soon after bolting. An approximately 1 cm region at
522 the apex of the stem was placed in apex culture medium (ACM: ½ MS medium, 1% [w/v]
523 sucrose, pH adjusted to 5.8 with 1M KOH, 0.8% [w/v] agarose, supplemented with 1X
524 vitamins (1000X stock: 5 g myo-inositol, 0.05 g nicotinic acid, 640.05 g pyridoxine
525 hydrochloride (B6), 0.5 g thiamine hydrochloride (B1), 0.1 g glycine, H_2O to 50 mL, filter
526 before aliquoting) and cytokinins (BAP; 125-175 nM final)), and flower buds were removed
527 until the shoot meristem was sufficiently exposed for proper imaging. Dissected samples
528 were placed in a growth cabinet under long-day conditions until confocal observation.
529
530 *Confocal imaging*
531 Imaging was carried out on a Leica TCS SP8 (DM6000 CS) upright confocal laser scanning
532 microscope, equipped with a 25x water dipping lens (Leica HC FLUOTAR L 25x/0.95 W
533 VISIR) and a Leica HyD hybrid detector. Either plants expressed the *pUBQ10::LTI6b-*
534 *TdTomato* fluorescent plasma membrane marker, or FM4-64 (ThermoFisher Scientific,
535 T13320) was used to mark the plasma membrane as previously described (Fernandez et
536 al., 2010). FM4-64 was excited with a 488 nm laser diode and detected at 600-640 nm. GFP
537 was excited at 488 nm and detected at 500-520 nm. VENUS was excited at 514 nm and

538 detected at 520-535 nm. tdTomato was excited at either 514 or 552 nm and detected at 560-
539 600 nm.
540
541 *Image analysis*
542 Fiji (Schindelin et al., 2012) was used to generate 2D projections from 3D confocal stacks
543 (3D viewer plugin) and to generate orthogonal slices.
544
545 The MultiAngle Reconstruction and Segmentation (MARS) pipeline (Fernandez et al., 2010)
546 was used to generate 3D reconstructions of confocal stacks. For this, shoot meristems were
547 imaged from multiple angles by means of a custom-made device to tilt and/or rotate the
548 sample by 15-20 degrees between acquisitions. After fusion using MARS, the external
549 contours of the sample were detected using the Level Set Method (Kiss et al., 2017) and
550 this contour was then used to segment the 3D reconstructed sample using a watershed
551 segmentation algorithm. Cells were then extracted from the segmented image for the L1
552 and L2 tissue layers and the volume of each cell was calculated.
553
554 MorphoGraphX (Barbier de Reuille et al., 2015; Kiss et al., 2017) was used to measure cell
555 size, growth and curvature for individual image stacks. For cell size, we determined the
556 image slice within the L1 and L2 layers that was orthogonal to the axis of acquisition, and
557 which contained the midline of the group of cells near the centre of the image (in order to
558 avoid cells that had been imaged from the side). We then segmented and extracted cell
559 areas. For growth, we first identified the tissue surface, generated the mesh, projected signal
560 from the first cell layer (usually 5.5-6 μm), watershed-segmented the mesh, and determined
561 cell lineages over two or more time points. Minimal curvature was calculated within a 10-μm
562 radius for each point in the image, and for segmented tissues, was then normalised to the
563 size of each cell. R was used to plot the data and run statistical tests.
564
565 *Statistical analysis*
566 Plots and statistical analyses were done with R studio version 2023.03.0 (Posit team, 2023)
567 using the *ggplot2* package (Wickham, H., 2016). Welch's t-tests were used to compare the
568 mean of two independent groups: cell areas and cell volumes in different cell layers, and the
569 apparent Young's modulus in WT and mutant SAM. When we use boxplots, the boxes
570 extend from the first to the third quartile and the whiskers from 10% to 90% of the values,
571 the solid black line represents the median of the distribution. Throughout the manuscript,
572 average values are means $\pm$ s.d. On scatter plots, the regression line represents the best

573 linear fit of the data, along with its 95% confidence interval. Pearson's correlation coefficients
574 and the related p-values were calculated with *ggplot2*.
575
576 *Analytical models*
577 We used a morphoelastic framework, which involves a multiplicative decomposition of the
578 deformation gradient into growth tensor, describing changes in mass or density, and an
579 elastic tensor, accounting for the elastic material response, commonly used in the literature
580 (Goriely and Ben Amar, 2005; Moulton et al., 2013). The outer L1 layer of cells in the SAM
581 is modelled as a planar elastic rod attached to an elastic foundation that represents the inner
582 layers (Almet et al., 2019; Moulton et al., 2013) (Fig. S2). The elastic rod grows axially in the
583 x-direction, which generates compressive stresses due to clamped boundary conditions at
584 the two rod ends. These stresses lead to instability, and buckling that result in the formation
585 of folded structures, which closely resemble the shapes obtained in our experimental data.
586 We used the model to explore differences in the growth rates and stiffness in the L1 and L2
587 layers of the various groups in our study (see supplementary methods for details).
588
589 *Atomic force microscopy (AFM) and data analysis*
590 Meristems were dissected to remove all flower buds older than stage 3 the day before AFM
591 observations and placed in ACM in 60 mm plastic Petri dishes. Acquisitions were carried out
592 in distilled water at room temperature on a stand-alone JPK Nanowizard III microscope
593 equipped with a CellHesion module (100 µm-range Z-piezo) using the Quantitative Imaging
594 mode (QI). We used a silica spherical tip with a radius of 400 nm (Special Development SD-
595 sphere-NCH, Nanosensors) mounted on a silicon cantilever with a nominal force constant
596 of 42 $N.m^{-1}$. Scan size was generally a square field of 45 x 45 µm with pixel size of
597 approximately 500 nm. An applied force trigger of 1 µN was used in order to indent only the
598 cell wall (Milani et al., 2011; Tvergaard and Needleman, 2018), with a ramp size of 2 µm, an
599 approach speed of 10 $\mu m.s^{-1}$ and a retraction speed of 100 $\mu m.s^{-1}$. Apparent Young's
600 modulus was obtained by fitting the first 100-150 nm of the force displacement curve with a
601 Hertz model and subsequently corrected for the effect of slope (see supplementary
602 methods).
603
604 *RNA in situ hybridisations*
605 RNA *in situ* hybridisations on sections were performed according to published protocols
606 (Long et al., 1996). Meristems were dissected just after bolting, fixed in FAA (formaldehyde
607 3.7% [v/v], ethanol 50% [v/v], acetic acid 5% [v/v], H_2O to final volume), washed, dehydrated

608 and embedded in paraplast. Embedded samples were cut (10 µm-thick) and attached to
609 pre-coated glass slides (Superfrost Plus Gold, Fisher Scientific). Antisense probes were
610 made from PCR products using cDNA from inflorescences as a template, except for *CLV3*,
611 which was amplified using genomic DNA (see supplementary methods for detailed primer
612 list). Those PCR products were transcribed into RNA and then labelled using digoxigenin
613 (DIG)-UTP. All probes were filtered on columns (CHROMA SPIN-30 columns, Clontech) to
614 remove remaining nucleotides. Immunodetection was performed using an anti-DIG antibody
615 coupled to alkaline phosphatase (Anti-Digoxygenin-AP, Fab fragments, Roche), whose
616 activity was detected by the chromogenic method using NBT/BCIP (Roche). Sections were
617 finally washed with water and observed under a Zeiss Imager M2 microscope equipped with
618 an AxioCam Mrc camera, and 10 X or 20 X objectives in DIC (differential interference
619 contrast) mode.
620
621 *Hormone treatments*
622 Auxin treatments were performed by immersing dissected SAM in 1 or 2 mM Indole-3-acetic
623 acid (IAA) solution (Sigma) for five hours as described (Galvan-Ampudia et al., 2020). *DR5*
624 reporter expression was monitored in the samples by confocal microscopy approximately
625 24 hours post-treatment. Treatments were carried out on *clv1-8* (in the Col-0 accession, as
626 in Fig. S9D, E), *clv3-2* plants (in the L*er* accession, as in Fig. S9A, B), or in F1 plants of a
627 cross between *clv3-2* and *clv3-21* (mixed Col-0 and L*er* background, as in Fig. 6C-D, I-L).
628
629 **Acknowledgements**
630 We thank V. Mirabet and N. Dubrulle for help with preliminary AFM measurements, A. Kiss
631 for help with 3D segmentations and surface curvature detection, Zofia Haftek-Terreau and
632 G. Gilbert for help with *in situ* hybridisations, and Aurélie Chauvet for help with molecular
633 biology. We thank the PLATIM/LyMIC imaging facility of the SFR Biosciences
634 (UMS3444/CNRS, US8/Inserm, ENS de Lyon, UCBL1). We thank A. Lacroix, J. Berger, P.
635 Bolland, H. Leyral, and I. Desbouchages for assistance with plant growth and logistics. This
636 article is based on LRL's PhD thesis: Rambaud-Lavigne, L. E. S. (2018), The genetics and
637 mechanics of stem cells at the Arabidopsis shoot apex. *PhD thesis*, University of Lyon, Lyon,
638 France, downloadable at: theses.hal.science/tel-02366972.
639
640 **Author contributions**
641 Conceptualization: LRL, AB, PD; Methodology: AC, NG, SB, AB; Software & Modeling: AC,
642 NG; Validation: LRL, VB, PD; Formal Analysis: QL, AC, LRL, PD; Investigation: LRL, SB,

VB, PD; Data Curation: LRL, PD; Writing - Original Draft Preparation: LRL, AC, NG, PD; Writing - Review & Editing: LRL, AC, SB, NG, AB, PD; Visualisation: LRL, AC, QL, NG, PD; Supervision: NG, AB, PD; Funding Acquisition: LRL, NG, PD.

Competing interests

No competing interests declared.

Funding

This work was supported by a PhD fellowship from the Ecole Normale Supérieure de Lyon to LRL., and a Science Engineering Research Board grant (SERB-POWER) to NG.

Data availability

All datasets and scripts will be made available before publication (online repository).

References

Abbasi, N., Park, Y.-I. and Choi, S.-B. (2011). Pumilio Puf domain RNA-binding proteins in Arabidopsis. *Plant Signal. Behav.* **6**, 364–368.

Aggarwal, P., Yadav, R. K. and Reddy, G. V. (2010). Identification of novel markers for stem-cell niche of Arabidopsis shoot apex. *Gene Expr. Patterns* **10**, 259–264.

Almet, A. A., Byrne, H. M., Maini, P. K. and Moulton, D. E. (2019). Post-buckling behaviour of a growing elastic rod. *J. Math. Biol.* **78**, 777–814.

Banwarth-Kuhn, M., Rodriguez, K., Michael, C., Ta, C.-K., Plong, A., Bourgain-Chang, E., Nematbakhsh, A., Chen, W., Roy-Chowdhury, A., Reddy, G. V., et al. (2022). Combined computational modeling and experimental analysis integrating chemical and mechanical signals suggests possible mechanism of shoot meristem maintenance. *PLOS Comput. Biol.* **18**, e1010199.

Barbier de Reuille, P., Routier-Kierzkowska, A.-L., Kierzkowski, D., Bassel, G. W., Schüpbach, T., Tauriello, G., Bajpai, N., Strauss, S., Weber, A., Kiss, A., et al. (2015). MorphoGraphX: A platform for quantifying morphogenesis in 4D. *eLife* **4**, 05864.

Battogtokh, D. and Tyson, J. J. (2022). Nucleation of stem cell domains in a bistable activator-inhibitor model of the shoot apical meristem. *Chaos Woodbury N* **32**, 093117.

Beauzamy, L., Louveaux, M., Hamant, O. and Boudaoud, A. (2015). Mechanically, the Shoot Apical Meristem of Arabidopsis Behaves like a Shell Inflated by a Pressure of About 1 MPa. *Front. Plant Sci.* **6**,.

Berleth, T. and Jürgens, G. (1993). The role of the monopteros gene in organising the basal body region of the Arabidopsis embryo. *Development* **118**, 575–587.

Bhatia, N., Bozorg, B., Larsson, A., Ohno, C., Jönsson, H. and Heisler, M. G. (2016). Auxin Acts through MONOPTEROS to Regulate Plant Cell Polarity and Pattern Phyllotaxis. *Curr. Biol.*

680 **26**, 3202–3208.
681 **Brand, U., Fletcher, J. C., Hobe, M., Meyerowitz, E. M. and Simon, R.** (2000). Dependence of
682 Stem Cell Fate in Arabidopsis on a Feedback Loop Regulated by CLV3 Activity. *Science* **289**, 617–
683 619.
684 **Brand, U., Grünewald, M., Hobe, M. and Simon, R.** (2002). Regulation of CLV3 Expression by
685 Two Homeobox Genes in Arabidopsis. *Plant Physiol.* **129**, 565–575.
686 **Busch, W., Miotk, A., Ariel, F. D., Zhao, Z., Forner, J., Daum, G., Suzaki, T., Schuster, C.,**
687 **Schultheiss, S. J., Leibfried, A., et al.** (2010). Transcriptional Control of a Plant Stem Cell Niche.
688 *Dev. Cell* **18**, 841–853.
689 **Cheng, Y., Dai, X. and Zhao, Y.** (2006). Auxin biosynthesis by the YUCCA flavin
690 monooxygenases controls the formation of floral organs and vascular tissues in Arabidopsis.
691 *Genes Dev.* **20**, 1790–1799.
692 **Chickarmane, V. S., Gordon, S. P., Tarr, P. T., Heisler, M. G. and Meyerowitz, E. M.** (2012).
693 Cytokinin signaling as a positional cue for patterning the apical–basal axis of the growing
694 Arabidopsis shoot meristem. *Proc. Natl. Acad. Sci. U. S. A.* **109**, 4002–4007.
695 **Clark, S. E., Running, M. P. and Meyerowitz, E. M.** (1993). CLAVATA1, a regulator of meristem
696 and flower development in Arabidopsis. *Development* **119**, 397–418.
697 **Clark, S. E., Running, M. P. and Meyerowitz, E. M.** (1995). CLAVATA3 is a specific regulator of
698 shoot and floral meristem development affecting the same processes as CLAVATA1. *Development*
699 **121**, 2057–2067.
700 **Clark, S. E., Williams, R. W. and Meyerowitz, E. M.** (1997). The CLAVATA1 gene encodes a
701 putative receptor kinase that controls shoot and floral meristem size in Arabidopsis. *Cell* **89**, 575–
702 585.
703 **Dao, T. Q., Weksler, N., Liu, H. M.-H., Leiboff, S. and Fletcher, J. C.** (2022). Interactive CLV3,
704 CLE16 and CLE17 signaling mediates stem cell homeostasis in the Arabidopsis shoot apical
705 meristem. *Development* **149**, dev200787.
706 **Daum, G., Medzihradszky, A., Suzaki, T. and Lohmann, J. U.** (2014). A mechanistic framework
707 for noncell autonomous stem cell induction in Arabidopsis. *Proc. Natl. Acad. Sci.* **111**, 14619–
708 14624.
709 **de Reuille, P. B., Bohn-Courseau, I., Ljung, K., Morin, H., Carraro, N., Godin, C. and Traas, J.**
710 (2006). Computer simulations reveal properties of the cell-cell signaling network at the shoot apex
711 in Arabidopsis. *Proc. Natl. Acad. Sci. U. S. A.* **103**, 1627–1632.
712 **Douady, S. and Couder, Y.** (1996). Phyllotaxis as a Dynamical Self Organizing Process Part II:
713 The Spontaneous Formation of a Periodicity and the Coexistence of Spiral and Whorled Patterns.
714 *J. Theor. Biol.* **178**, 275–294.
715 **Fernandez, R., Das, P., Mirabet, V., Moscardi, E., Traas, J., Verdeil, J.-L., Malandain, G. and**
716 **Godin, C.** (2010). Imaging plant growth in 4D: robust tissue reconstruction and lineaging at cell
717 resolution. *Nat. Methods* **7**, 547–553.

718 **Fletcher, J. C., Brand, U., Running, M. P., Simon, R. and Meyerowitz, E. M.** (1999). Signaling of
719 Cell Fate Decisions by CLAVATA3 in Arabidopsis Shoot Meristems. *Science* **283**, 1911–1914.
720 **Friml, J., Vieten, A., Sauer, M., Weijers, D., Schwarz, H., Hamann, T., Offringa, R. and**
721 **Jürgens, G.** (2003). Efflux-dependent auxin gradients establish the apical–basal axis of
722 Arabidopsis. *Nature* **426**, 147–153.
723 **Fujita, M., Himmelspach, R., Hocart, C. H., Williamson, R. E., Mansfield, S. D. and**
724 **Wasteneys, G. O.** (2011). Cortical microtubules optimize cell-wall crystallinity to drive
725 unidirectional growth in Arabidopsis. *Plant J.* **66**, 915–928.
726 **Galvan-Ampudia, C. S., Cerutti, G., Legrand, J., Brunoud, G., Martin-Arevalillo, R., Azais, R.,**
727 **Bayle, V., Moussu, S., Wenzl, C., Jaillais, Y., et al.** (2020). Temporal integration of auxin
728 information for the regulation of patterning. *eLife* **9**, e55832.
729 **Gordon, S. P., Chickarmane, V. S., Ohno, C. and Meyerowitz, E. M.** (2009). Multiple feedback
730 loops through cytokinin signaling control stem cell number within the Arabidopsis shoot meristem.
731 *Proc. Natl. Acad. Sci.* **106**, 16529–16534.
732 **Goriely, A.** (2017). *The Mathematics and Mechanics of Biological Growth*. New York, NY: Springer
733 New York.
734 **Goriely, A. and Ben Amar, M.** (2005). Differential Growth and Instability in Elastic Shells. *Phys.*
735 *Rev. Lett.* **94**, 198103.
736 **Gruel, J., Landrein, B., Tarr, P., Schuster, C., Refahi, Y., Sampathkumar, A., Hamant, O.,**
737 **Meyerowitz, E. M. and Jo nsson, H.** (2016). An epidermis-driven mechanism positions and
738 scales stem cell niches in plants. *Sci. Adv.* **2**, e1500989–e1500989.
739 **Hardtke, C. S. and Berleth, T.** (1998). The Arabidopsis gene MONOPTEROS encodes a
740 transcription factor mediating embryo axis formation and vascular development. *EMBO J.* **17**,
741 1405–1411.
742 **Heisler, M. G., Ohno, C., Das, P., Sieber, P., Reddy, G. V., Long, J. A. and Meyerowitz, E. M.**
743 (2005). Patterns of Auxin Transport and Gene Expression during Primordium Development
744 Revealed by Live Imaging of the Arabidopsis Inflorescence Meristem. *Curr. Biol.* **15**, 1899–1911.
745 **Hervieux, N., Dumond, M., Sapala, A., Routier-Kierzkowska, A.-L., Kierzkowski, D., Roeder,**
746 **A. H. K., Smith, R. S., Boudaoud, A. and Hamant, O.** (2016). A Mechanical Feedback Restricts
747 Sepal Growth and Shape in Arabidopsis. *Curr. Biol.*
748 **Hong, L., Dumond, M., Tsugawa, S., Sapala, A., Routier-Kierzkowska, A.-L., Zhou, Y., Chen,**
749 **C., Kiss, A., Zhu, M., Hamant, O., et al.** (2016). Variable Cell Growth Yields Reproducible Organ
750 Development through Spatiotemporal Averaging. *Dev. Cell* **38**, 15–32.
751 **Jeong, S., Trotochaud, A. E. and Clark, S. E.** (1999). The Arabidopsis CLAVATA2 Gene
752 Encodes a Receptor-like Protein Required for the Stability of the CLAVATA1 Receptor-like Kinase.
753 *Plant Cell* **11**, 1925–1933.
754 **John, A., Smith, E. S., Jones, D. S., Soyars, C. L. and Nimchuk, Z. L.** (2023). A network of
755 CLAVATA receptors buffers auxin-dependent meristem maintenance. *Nat. Plants* **9**, 1306–1317.

Jones, D. S., John, A., VanDerMolen, K. R. and Nimchuk, Z. L. (2020). CLAVATA Signaling Ensures Reproductive Development in Plants across Thermal Environments. *Curr. Biol.*

Jönsson, H., Heisler, M., Reddy, G. V., Agrawal, V., Gor, V., Shapiro, B. E., Mjolsness, E. and Meyerowitz, E. M. (2005). Modeling the organization of the WUSCHEL expression domain in the shoot apical meristem. *Bioinforma. Oxf. Engl.* **21 Suppl 1**, i232-240.

Jönsson, H., Heisler, M. G., Shapiro, B. E., Meyerowitz, E. M. and Mjolsness, E. (2006). An auxin-driven polarized transport model for phyllotaxis. *Proc. Natl. Acad. Sci. U. S. A.* **103**, 1633–1638.

Kamimoto, K., Kaneko, K., Kok, C. Y.-Y., Okada, H., Miyajima, A. and Itoh, T. (2016). Heterogeneity and stochastic growth regulation of biliary epithelial cells dictate dynamic epithelial tissue remodeling. *eLife* **5**, e15034.

Kayes, J. M. and Clark, S. E. (1998). CLAVATA2, a regulator of meristem and organ development in Arabidopsis. *Development* **125**, 3843–3851.

Kinoshita, A., Seo, M., Kamiya, Y. and Sawa, S. (2015). Mystery in genetics: PUB4 gives a clue to the complex mechanism of CLV signaling pathway in the shoot apical meristem. *Plant Signal. Behav.* **10**, e1028707.

Kiss, A., Moreau, T., Mirabet, V., Calugaru, C. I., Boudaoud, A. and Das, P. (2017). Segmentation of 3D images of plant tissues at multiple scales using the level set method. *Plant Methods* **13**,.

Klawe, F. Z., Stiehl, T., Bastian, P., Gaillochet, C., Lohmann, J. U. and Marciniak-Czochra, A. (2020). Mathematical modeling of plant cell fate transitions controlled by hormonal signals. *PLoS Comput. Biol.* **16**, e1007523.

Kwon, C. S., Chen, C. and Wagner, D. (2005). WUSCHEL is a primary target for transcriptional regulation by SPLAYED in dynamic control of stem cell fate in Arabidopsis. *Genes Dev.* **19**, 992–1003.

Laufs, P., Grandjean, O., Jonak, C., Kiêu, K. and Traas, J. (1998). Cellular parameters of the shoot apical meristem in Arabidopsis. *Plant Cell Online* **10**, 1375–1389.

Laux, T., Mayer, K. F., Berger, J. and Jurgens, G. (1996). The WUSCHEL gene is required for shoot and floral meristem integrity in Arabidopsis. *Development* **122**, 87–96.

Lenhard, M. and Laux, T. (2003). Stem cell homeostasis in the Arabidopsis shoot meristem is regulated by intercellular movement of CLAVATA3 and its sequestration by CLAVATA1. *Development* **130**, 3163–3173.

Lindsay, D. L., Sawhney, V. K. and Bonham-Smith, P. C. (2006). Cytokinin-induced changes in CLAVATA1 and WUSCHEL expression temporally coincide with altered floral development in Arabidopsis. *Plant Sci.* **170**, 1111–1117.

Long, J. A., Moan, E. I., Medford, J. I. and Barton, M. K. (1996). A member of the KNOTTED class of homeodomain proteins encoded by the STM gene of Arabidopsis. *Nature* **379**, 66–69.

Long, Y., Cheddadi, I., Mosca, G., Mirabet, V., Dumond, M., Kiss, A., Traas, J., Godin, C. and

794 **Boudaoud, A.** (2020). Cellular Heterogeneity in Pressure and Growth Emerges from Tissue
795 Topology and Geometry. *Curr. Biol.* **30**, 1504-1516.e8.
796 **Luo, L., Zeng, J., Wu, H., Tian, Z. and Zhao, Z.** (2018). A Molecular Framework for Auxin-
797 Controlled Homeostasis of Shoot Stem Cells in Arabidopsis. *Mol. Plant* **11**, 899–913.
798 **Mayer, K. F., Schoof, H., Haecker, A., Lenhard, M., Jürgens, G. and Laux, T.** (1998). Role of
799 WUSCHEL in regulating stem cell fate in the Arabidopsis shoot meristem. *Cell* **95**, 805–815.
800 **Medford, J. I., Behringer, F. J., Callos, J. D. and Feldmann, K. A.** (1992). Normal and abnormal
801 development in the Arabidopsis vegetative shoot apex. *Plant Cell* **4**, 631–643.
802 **Michael, C., Banwarth-Kuhn, M., Rodriguez, K., Ta, C.-K., Roy-Chowdhury, A., Chen, W.,**
803 **Venugopala Reddy, G. and Alber, M.** (2023). Role of turgor-pressure induced boundary tension
804 in the maintenance of the shoot apical meristem of Arabidopsis thaliana. *J. R. Soc. Interface* **20**,
805 20230173.
806 **Milani, P., Gholamirad, M., Traas, J., Arnéodo, A., Boudaoud, A., Argoul, F. and Hamant, O.**
807 (2011). In vivo analysis of local wall stiffness at the shoot apical meristem in Arabidopsis using
808 atomic force microscopy: Measuring wall stiffness in meristems with AFM. *Plant J.* **67**, 1116–1123.
809 **Milani, P., Mirabet, V., Cellier, C., Rozier, F., Hamant, O., Das, P. and Boudaoud, A.** (2014).
810 Matching Patterns of Gene Expression to Mechanical Stiffness at Cell Resolution through
811 Quantitative Tandem Epifluorescence and Nanoindentation. *PLANT Physiol.* **165**, 1399–1408.
812 **Miwa, H., Betsuyaku, S., Iwamoto, K., Kinoshita, A., Fukuda, H. and Sawa, S.** (2008). The
813 Receptor-Like Kinase SOL2 Mediates CLE Signaling in Arabidopsis. *Plant Cell Physiol.* **49**, 1752–
814 1757.
815 **Moulton, D. E., Lessinnes, T. and Goriely, A.** (2013). Morphoelastic rods. Part I: A single
816 growing elastic rod. *J. Mech. Phys. Solids* **61**, 398–427.
817 **Müller, R., Borghi, L., Kwiatkowska, D., Laufs, P. and Simon, R.** (2006). Dynamic and
818 Compensatory Responses of Arabidopsis Shoot and Floral Meristems to CLV3 Signaling. *Plant*
819 *Cell* **18**, 1188–1198.
820 **Müller, R., Bleckmann, A. and Simon, R.** (2008). The Receptor Kinase CORYNE of *Arabidopsis*
821 Transmits the Stem Cell–Limiting Signal CLAVATA3 Independently of CLAVATA1. *Plant Cell*
822 *Online* **20**, 934–946.
823 **Nemec-Venza, Z., Madden, C., Stewart, A., Liu, W., Novák, O., Pěnčík, A., Cuming, A. C.,**
824 **Kamisugi, Y. and Harrison, C. J.** (2022). CLAVATA modulates auxin homeostasis and transport
825 to regulate stem cell identity and plant shape in a moss. *New Phytol.* **234**, 149–163.
826 **Nimchuk, Z. L., Tarr, P. T., Ohno, C., Qu, X. and Meyerowitz, E. M.** (2011). Plant Stem Cell
827 Signaling Involves Ligand-Dependent Trafficking of the CLAVATA1 Receptor Kinase. *Curr. Biol.*
828 **21**, 345–352.
829 **Plong, A., Rodriguez, K., Alber, M., Chen, W. and Reddy, G. V.** (2021). CLAVATA3 mediated
830 simultaneous control of transcriptional and post-translational processes provides robustness to the
831 WUSCHEL gradient. *Nat. Commun.* **12**, 6361.

832 **Posit team** (2023). RStudio: Integrated Development Environment for R. Posit Software, PBC,
833 Boston, MA. URL http://www.posit.co/.
834 **Qiu, C., Dutcher, R. C., Porter, D. F., Arava, Y., Wickens, M. and Hall, T. M. T.** (2019). Distinct
835 RNA-binding modules in a single PUF protein cooperate to determine RNA specificity. *Nucleic*
836 *Acids Res.* gkz583.
837 **Reddy, G. V. and Meyerowitz, E. M.** (2005). Stem-Cell Homeostasis and Growth Dynamics Can
838 Be Uncoupled in the Arabidopsis Shoot Apex. *Science* **310**, 663–667.
839 **Reinhardt, D., Mandel, T. and Kuhlemeier, C.** (2000). Auxin Regulates the Initiation and Radial
840 Position of Plant Lateral Organs. *Plant Cell* **12**, 507–518.
841 **Sampathkumar, A., Peaucelle, A., Fujita, M., Schuster, C., Persson, S., Wasteneys, G. O. and**
842 **Meyerowitz, E. M.** (2019). Primary wall cellulose synthase regulates shoot apical meristem
843 mechanics and growth. *Development* dev.179036.
844 **Schindelin, J., Arganda-Carreras, I., Frise, E., Kaynig, V., Longair, M., Pietzsch, T., Preibisch,**
845 **S., Rueden, C., Saalfeld, S., Schmid, B., et al.** (2012). Fiji: an open-source platform for biological-
846 image analysis. *Nat. Methods* **9**, 676–682.
847 **Schlegel, J., Denay, G., Wink, R. H., Pinto, K. G., Stahl, Y., Schmid, J., Blümke, P. and Simon,**
848 **R. G.** (2021). Control of Arabidopsis shoot stem cell homeostasis by two antagonistic CLE peptide
849 signalling pathways. *eLife* **10**, e70934.
850 **Schoof, H., Lenhard, M., Haecker, A., Mayer, K. F. X., Jürgens, G. and Laux, T.** (2000). The
851 Stem Cell Population of Arabidopsis Shoot Meristems Is Maintained by a Regulatory Loop between
852 the CLAVATA and WUSCHEL Genes. *Cell* **100**, 635–644.
853 **Schuster, C., Gaillochet, C., Medzihradszky, A., Busch, W., Daum, G., Krebs, M., Kehle, A.**
854 **and Lohmann, J. U.** (2014). A Regulatory Framework for Shoot Stem Cell Control Integrating
855 Metabolic, Transcriptional, and Phytohormone Signals. *Dev. Cell* **28**, 438–449.
856 **Shapiro, B. E., Tobin, C., Mjolsness, E. and Meyerowitz, E. M.** (2015). Analysis of cell division
857 patterns in the *Arabidopsis* shoot apical meristem. *Proc. Natl. Acad. Sci.* **112**, 4815–4820.
858 **Shi, B., Guo, X., Wang, Y., Xiong, Y., Wang, J., Hayashi, K., Lei, J., Zhang, L. and Jiao, Y.**
859 (2018). Feedback from Lateral Organs Controls Shoot Apical Meristem Growth by Modulating
860 Auxin Transport. *Dev. Cell* **44**, 204-216.e6.
861 **Shimada, T. L., Shimada, T. and Hara-Nishimura, I.** (2010). A rapid and non-destructive
862 screenable marker, FAST, for identifying transformed seeds of Arabidopsis thaliana. *Plant J.* **61**,
863 519–528.
864 **Stuttmann, J., Barthel, K., Martin, P., Ordon, J., Erickson, J. L., Herr, R., Ferik, F.,**
865 **Kretschmer, C., Berner, T., Keilwagen, J., et al.** (2021). Highly efficient multiplex editing: one-
866 shot generation of 8× Nicotiana benthamiana and 12× Arabidopsis mutants. *Plant J.* **106**, 8–22.
867 **Taguchi-Shiobara, F.** (2001). The fasciated ear2 gene encodes a leucine-rich repeat receptor-like
868 protein that regulates shoot meristem proliferation in maize. *Genes Dev.* **15**, 2755–2766.
869 **Tam, P. P., Barrette-Ng, I. H., Simon, D. M., Tam, M. W., Ang, A. L. and Muench, D. G.** (2010).

870 The Puf family of RNA-binding proteins in plants: phylogeny, structural modeling, activity and
871 subcellular localization. *BMC Plant Biol.* **10**, 44.
872 **Tsugawa, S., Hervieux, N., Kierzkowski, D., Routier-Kierzkowska, A.-L., Sapala, A., Hamant,**
873 **O., Smith, R. S., Roeder, A. H. K., Boudaoud, A. and Li, C.-B.** (2017). Clones of cells switch
874 from reduction to enhancement of size variability in Arabidopsis sepals. *Development* **144**, 4398–
875 4405.
876 **Tvergaard, V. and Needleman, A.** (2018). Effect of Properties and Turgor Pressure on the
877 Indentation Response of Plant Cells. *J. Appl. Mech.*
878 **Vernoux, T., Kronenberger, J., Grandjean, O., Laufs, P. and Traas, J.** (2000). PIN-FORMED 1
879 regulates cell fate at the periphery of the shoot apical meristem. *Development* **127**, 5157–5165.
880 **Vernoux, T., Brunoud, G., Farcot, E., Morin, V., Van den Daele, H., Legrand, J., Oliva, M.,**
881 **Das, P., Larrieu, A., Wells, D., et al.** (2011). The auxin signalling network translates dynamic input
882 into robust patterning at the shoot apex. *Mol. Syst. Biol.* **7**, 508.
883 **Whitewoods, C. D., Cammarata, J., Nemec Venza, Z., Sang, S., Crook, A. D., Aoyama, T.,**
884 **Wang, X. Y., Waller, M., Kamisugi, Y., Cuming, A. C., et al.** (2018). CLAVATA Was a Genetic
885 Novelty for the Morphological Innovation of 3D Growth in Land Plants. *Curr. Biol.*
886 **Wickham, H.** (2016). Ggplot2: Elegant graphics for data analysis (2nd ed.) Springer International
887 Publishing.
888 **Wu, X., Dabi, T. and Weigel, D.** (2005). Requirement of Homeobox Gene STIMPY/WOX9 for
889 Arabidopsis Meristem Growth and Maintenance. *Curr. Biol.* **15**, 436–440.
890 **Yadav, R. K., Girke, T., Pasala, S., Xie, M. and Reddy, G. V.** (2009). Gene expression map of the
891 Arabidopsis shoot apical meristem stem cell niche. *Proc. Natl. Acad. Sci.* **106**, 4941–4946.
892 **Yadav, R. K., Perales, M., Gruel, J., Girke, T., Jönsson, H. and Reddy, G. V.** (2011).
893 WUSCHEL protein movement mediates stem cell homeostasis in the Arabidopsis shoot apex.
894 *Genes Dev.* **25**, 2025–2030.
895 **Yamaguchi, N., Wu, M.-F., Winter, C. M., Berns, M. C., Nole-Wilson, S., Yamaguchi, A.,**
896 **Coupland, G., Krizek, B. A. and Wagner, D.** (2013). A molecular framework for auxin-mediated
897 initiation of flower primordia. *Dev. Cell* **24**, 271–282.
898 **Zhao, Z., Andersen, S. U., Ljung, K., Dolezal, K., Miotk, A., Schultheiss, S. J. and Lohmann,**
899 **J. U.** (2010). Hormonal control of the shoot stem-cell niche. *Nature* **465**, 1089–1092.

900 **Figure 1**

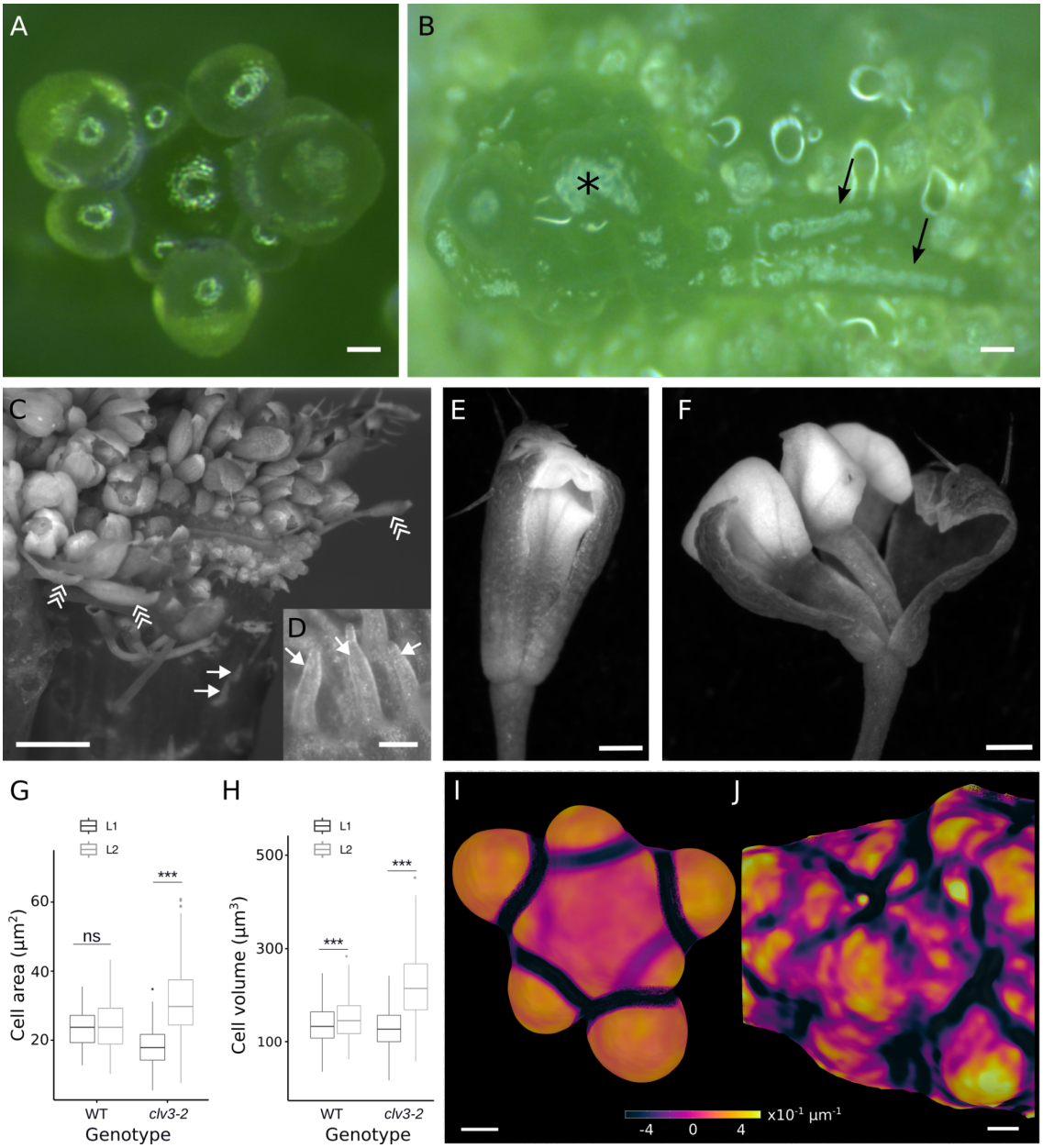

901

902 **Figure 1. Altered cell and tissue properties characterise fasciated SAM**

903 **(A, B)** Bright field images showing dissected WT L*er* (A) and *clv3-2* (B) SAM. The asterisk in (B)
904 shows the central outgrowth and arrows point out two linear elongations. **(C-F)** Bright field images
905 showing a dissected *clv3-21* SAM with filaments (arrows) on the side of the stem and abnormally
906 shaped flowers (arrowheads) (C), a close-up of the filaments (D), and *clv3-21* abnormally-shaped
907 flowers (E, F). **(G, H)** Boxplots of cell areas (G) or cell volumes (H) in the L1 (black) and L2 (grey)
908 cell layers of WT and *clv3-2* SAM. Mean ± s. d. areas (G) are 23.9 ± 5.8 μm^2 (WT L1) and 24.5 ±
909 7.2 μm^2 (WT L2); and 18.4 ± 5.3 μm^2 (*clv3* L1) and 31.2 ± 9.8 μm^2 (*clv3* L2). *P*-values (Welch's t-
910 test) = 0.545 (WT) and 4.65e-54 (*clv3-2*). n = 103 (L1) and 115 (L2) cells from 3 WT SAM; n = 400
911 (L1) and 244 (L2) cells from 3 *clv3-2* SAM. Mean ± s. d. volumes (H) are 136.5 ± 40.5 μm^3 (WT L1)
912 and 148.7 ± 44.5 μm^3 (WT L2); and 129.5 ± 40.9 μm^3 (*clv3* L1) and 249.1 ± 130.7 μm^3 (*clv3* L2). *P*-

913 values (Welch's t-test) = 2.32e-9 (WT) and 1.53e-204 (c*lv3-2*). n = 1468 (L1) and 529 (L2) cells from
914 4 WT SAM; 6426 (L1) and 3428 (L2) cells from 3 *clv3-2* SAM. **(I, J)** Colour maps quantifying minimal
915 curvature in representative WT Col-0 (I) and in *clv3-2* (J) SAM. The *clv3-2* SAM (J) is only a small
916 region of the entire meristem. Colourmap: warm helix (I, J). Scale bars: 30 µm (A, B, I, J), 1 mm (C),
917 200 µm (D), 100 µm (E, F).

Figure 2

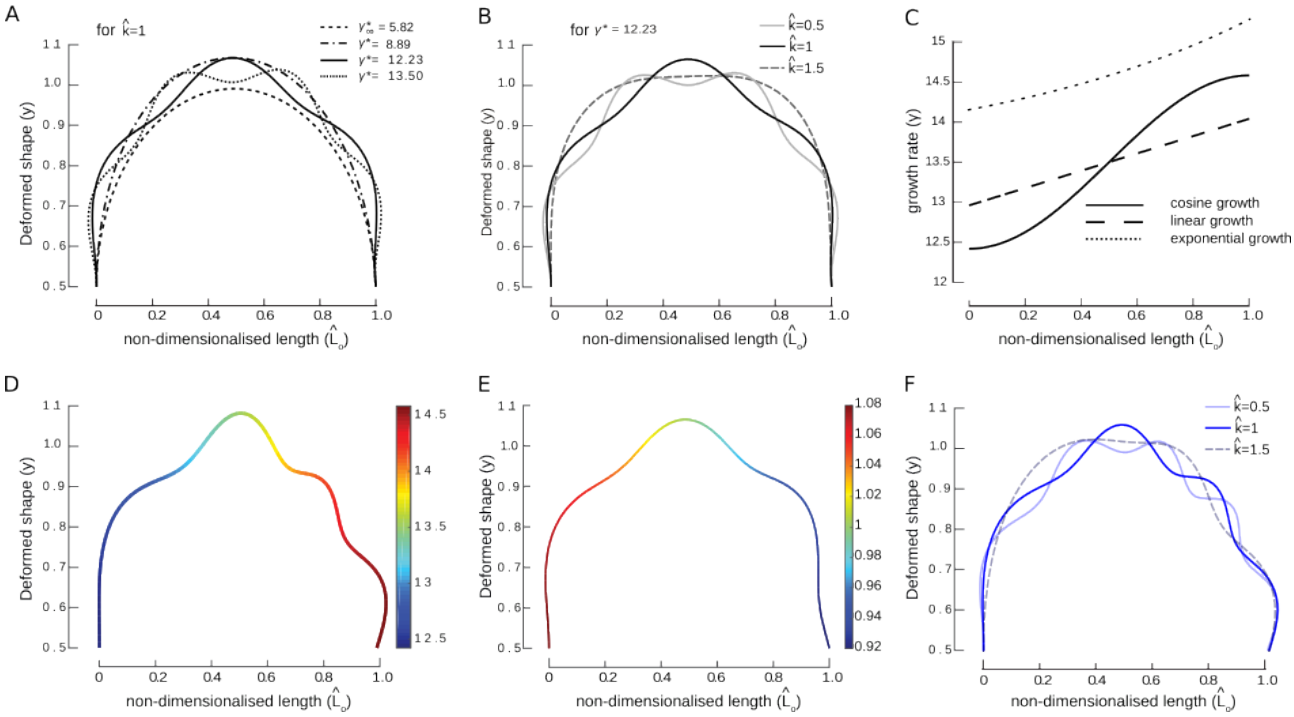

Figure 2. Growth and stiffness influence SAM shapes via growth-induced buckling

(A) Deformed shapes due to growth-induced buckling obtained for different values of critical growth rates (γ*) causing various buckling modes, with the stiffness of the underlying foundation fixed ($\hat{k}$ = 1). **(B)** Deformed shapes due to stiffness-induced buckling obtained for different values of foundation stiffness ($\hat{k}$ = 0.5, $\hat{k}$ = 1, $\hat{k}$ = 1.5), with the growth rate fixed (γ* = 12.23). **(C)** The choice of growth law affects the deformed shapes. We select three different forms of growth laws for the same value of growth rate γ_0: cosine, linear and exponential. **(D)** Deformed shape obtained as a result of growth-induced buckling in the case of cosine growth distribution. **(E)** Deformed shape obtained as a result of stiffness-induced buckling in the case of cosine stiffness distribution. **(F)** Effect of foundation stiffness on the asymmetric rod shapes obtained using growth heterogeneity.

931 **Figure 3**

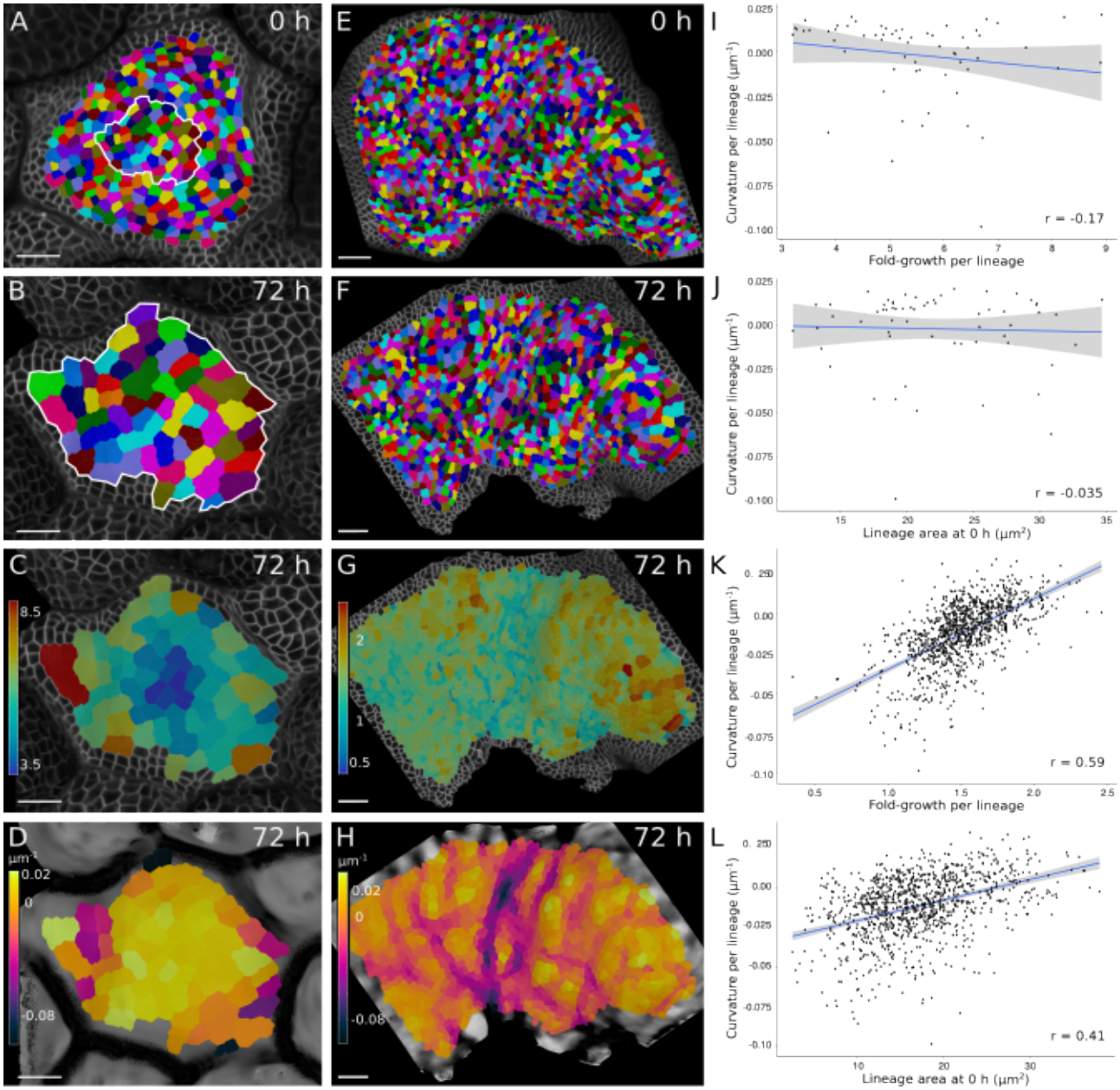

932

933 **Figure 3. Regional growth heterogeneities correlate with surface buckling in *clv* mutants**
934 **(A-H)** 3D surface reconstruction of a WT Col-0 (A-D) and a *clv3-7* (E-H) SAM, expressing the
935 *pUBQ10::Lti6b-tdTomato* membrane marker, at the start of the experiment (A, E) and 72 h later (B,
936 F). Solid white line in (A) and (B) delineates the same group of cells. Segmented cells are coloured
937 by lineage and outlines of unsegmented cells are shown. For each lineage, heatmaps for either
938 growth fold-change over 72 h (C, G) or minimal curvature (D, H) are represented on the second time
939 point. **(I-L)** Scatter plots of minimal curvature per lineage as a function of fold-growth per lineage (I,
940 K), or of minimal curvature per lineage as a function of initial lineage surface area (J, L) in WT (I, J)
941 and *clv3-7* (K, L) SAM. Regression lines representing the best fit are shown in blue, and confidence
942 intervals as shaded regions around them. n = 64 WT lineages (I, J); n = 1064 *clv3* lineages (K, L).
943 Pearson's correlation coefficients (r) are shown on the plots. *P*-values: $p = 0.18$ (I); $p = 0.79$ (J); $p <$
944 0.001 (K); $p < 0.001$ (L). Colourmap: Turbo (C, G); warm helix (D, H). Scale bars: 20 µm (A-H).

945 **Figure 4**

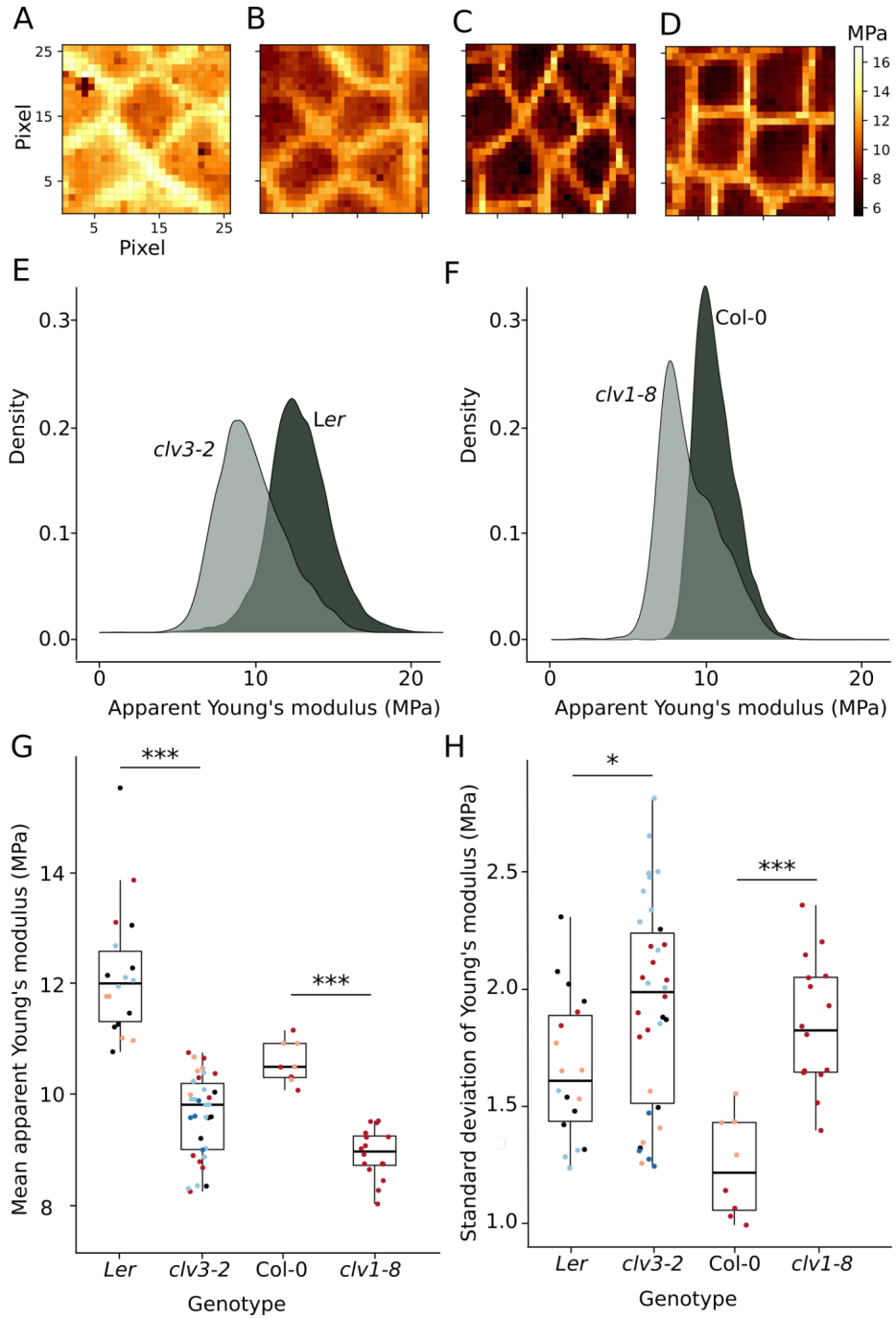

946

947 **Figure 4. Loss of *clv* is associated with reduced and heterogenous stiffness**

948 **(A-D)** Maps showing apparent Young's moduli derived from atomic force microscope scans of
949 representative L*er* (A), Col-0 (B), *clv3-2* (C), and *clv1-8* (D) SAM. **(E, F)** Density plots of apparent
950 Young's moduli from all probed WT (L*er*) and *clv3-2* (E), and WT (Col-0) and *clv1-8* (F) samples. **(G-**
951 **H)** Box plots of either mean values (G) or standard deviation values (H) of apparent Young's moduli
952 measurements of scans from all probed samples. Black dots show values of different samples
953 probed by a single scan, whereas coloured dots represent values from samples bearing multiple
954 non-overlapping scans, with each colour identifying an individual sample. Overall mean values
955 derived from individual mean apparent Young's moduli (G): L*er*, 12.2 ± 1.2 MPa; *clv3-2*, 9.7 ± 0.7;

956 Col-0, 10.58 ± 0.4; and *clv1-8*, 8.94 ± 0.5. Overall mean values derived from individual standard
957 deviations (H): L*er*, 1.7 ± 0.3 MPa; *clv3-2*, 1.9 ± 0.4; Col-0, 1.2 ± 0.2; *clv1-8*, 1.9 ± 0.3. *P*-values
958 (Welch's t-test): WT–*clv3*, 6.65e-8 and WT–*clv1*, 1.85e-7 (G); WT–*clv3*, 3.4e-2 and WT–*clv1*, 7.1e-
959 5 (H). n (non-overlapping scans/independent meristems): L*er*, 18/11; Col-0, 8/2; *clv3-2*, 34/8; and
960 *clv1-8*, 16/1.

961 **Figure 5**

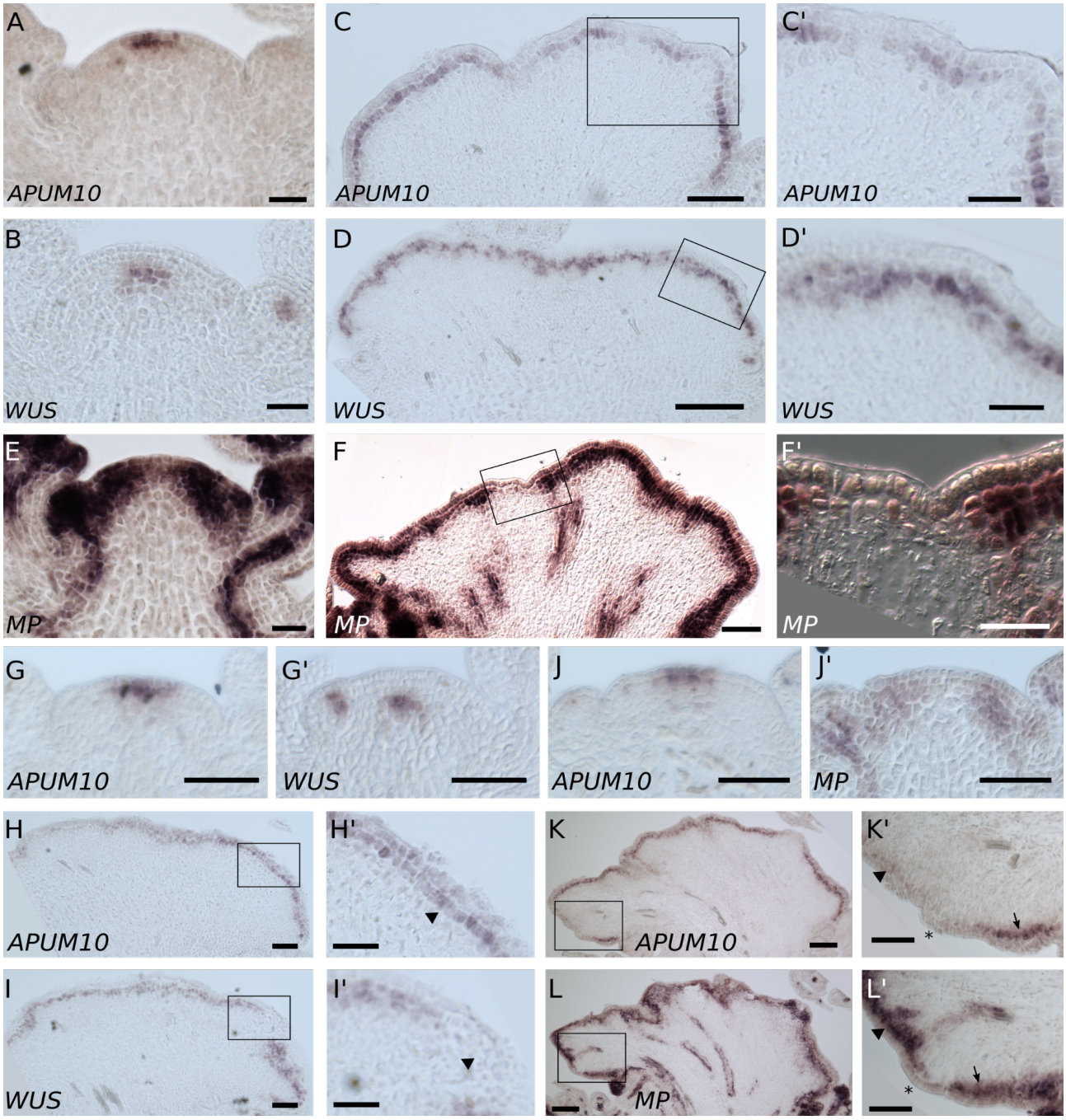

962

963 **Figure 5. Gene expression is heterogenous in *clv3* SAM**

964 **(A-F')** Pattern of mRNA localisation for *APUM10* (A, C, C'), *WUS* (B, D, D'), and *MP* (E-F') in WT
965 L*er* (A, B, E) or *clv3-2* (C, C', D, D', F, F') SAM. (C', D', and F') are magnified views of the boxed
966 regions in (C, D, and F), respectively. **(G-L')** Pairwise localisation of *APUM10* (G, J, H, H', K, K'),
967 *WUS* (G', I, I'), and *MP* (J', L, L') transcripts on alternating sections of meristems from individual WT
968 L*er* (G, G', J, J') or *clv3-2* (H-I', K-L') plants. Arrowheads (H',I', K', L') indicate zones where only one
969 of the two transcripts is detected, asterisks (K', L') indicate regions where neither is detected, and
970 arrows indicate areas where both are detected. (H', I', K', and L') are magnified views of the boxed
971 regions shown in (H, I, K, and L), respectively. Section thickness: 10 µm. Scale bars: 50 µm (A-C,
972 E, F, G, G', H', I', J, J', K', L'); 100 µm (D, H, I, K, L); 25 µm (C', D', F').

973 **Figure 6**

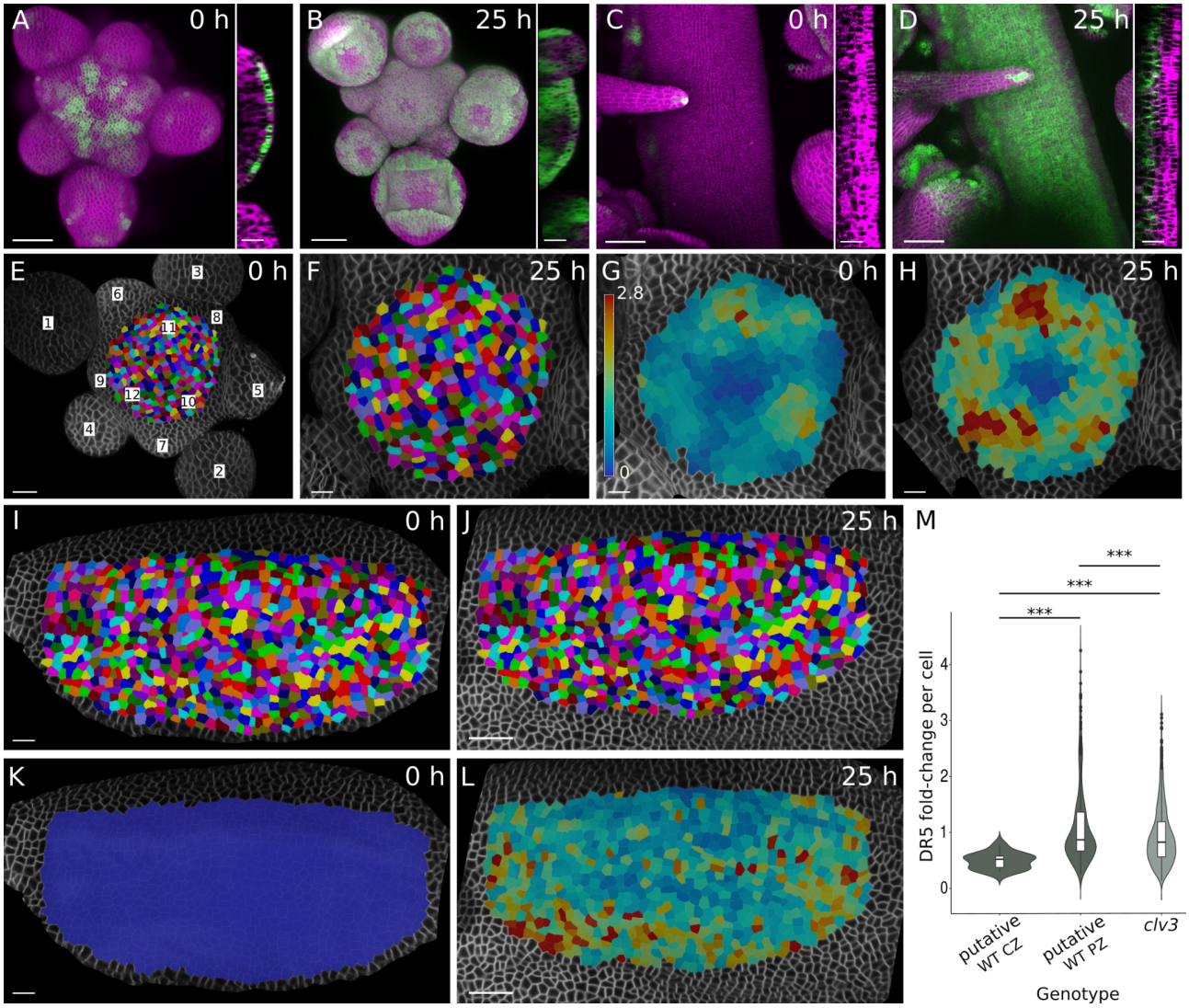

974

975 **Figure 6. *clv3* meristematic cells respond strongly to exogenous auxin treatment**
976 **(A-D)** Projections of confocal stacks showing the effect of IAA on WT Col-0 (A, B) and *clv3-2/clv3-*
977 *21* (C, D) SAM expressing the *pUBQ10::Lti6b-tdTomato* and *pDR5::GFPer* reporters. Samples are
978 shown either before (A, C) or 25 h after (B, D) a 5-hour IAA treatment. Orthogonal views of the SAM
979 are shown alongside each panel. n = 12 WT SAM (5 independent experiments), n = 11 *clv3* SAM (4
980 independent experiments). **(E-L)** Quantification of response to IAA treatment observed in
981 representative SAM from WT Col-0 (E-H) or *clv3-2/clv3-21* heterozygotes (I-L) carrying the
982 *pUBQ10::Lti6b-tdTomato* and *pDR5::GFPer* reporters. Views of the SAM surface before (E, I) and
983 after (F, J) treatment showing segmented cells coloured by lineage and unsegmented cells as grey
984 outlines. Numbers in (E) represent the phyllotactic order of flowers from oldest to youngest.
985 Heatmaps show DR5 signal per cell presented as a concentration (G, H, K, L) with a common colour
986 scale (G). **(M)** Violin plot reflecting distributions of DR5 fold-change per cell lineage between *clv3*
987 SAM and putative WT CZ and PZ (shown in E-L). *P*-values < 0.001 (Welch's t-test). n = 12 cells for
988 WT CZ; n = 300 cells for WT PZ; n = 713 cells for *clv3*. Colourmap: Turbo (G, H, K, L). Scale bars:
989 50 µm (top views in A-D); 20 µm (orthogonal sections in A-D, F-H, J, L); 10 µm (E, I, K).